

Vertical Structure and Driving Mechanism of PM_{2.5} and PM₁₀ Aerosols in Hefei Based on LiDAR Observations (2021–2023)

Yan Yan¹, Xueliang Deng^{1,2,*}, Rui Dai¹, Qianqian Xu¹, Qinqin Huang¹, Yang Liu¹, Chunxuan Wei¹,
Jinhua Xie¹, Yanfeng Li^{1,3}, & Yan Sun⁴

¹Hefei Meteorological Bureau, Hefei, Anhui 230061, China

²Heavy Rainfall Research Center of China, Wuhan Institute of Heavy Rain, China Meteorological Administration,
Wu Han, Hubei 430205, China

³Hefei Jichenyun Information Technology Co., Ltd., Hefei 230041, China

⁴Anhui Public Meteorological Service Center, Hefei, Anhui 230031, China

Correspondence to: Xueliang Deng (dengxueliang9989@aliyun.com)

Abstract:

Aerosol pollution remains a significant environmental concern in China. However, the vertical structure and evolution of particulate matter are poorly understood due to the lack of long-term, high-resolution observations. In Hefei, the aerosols during the study period were dominated by a mixture of fine particulate matter (PM_{2.5}) and coarse particulate matter (PM₁₀), mainly originating from urban traffic emissions, industrial activities, and regional transport, with significant contributions from secondary inorganic aerosols and occasional dust events. To address the knowledge gap in aerosol vertical distribution during different pollution episodes, this study employed an aerosol LiDAR system with 532 nm band to investigate the vertical profile characteristics of aerosols, with a focus on comparing the stratification differences of optical properties between PM_{2.5} and PM₁₀ pollution events over Hefei ~~across different periods and altitudes~~. The seasonal and diurnal variations of aerosol profiles were investigated, ~~and vertical structures were compared~~ on polluted and clean days. The relationship between near-surface particulate matter concentrations and ~~aerosol vertical properties aerosol stratification~~ was analyzed ~~at different heights~~, alongside the dynamic evolution of aerosol layers during typical pollution events. Our results demonstrated that the extinction coefficient (532 nm) of PM_{2.5}-polluted days below 0.6 km was approximately three times that of PM₁₀-polluted days.

28 In contrast, the depolarization ratio of PM₁₀-polluted episodes remains consistently higher than that of PM_{2.5}-polluted
 29 cases throughout the entire observed altitude range. The differences in extinction between polluted and clean days
 30 for PM_{2.5} were most pronounced below 0.9 km and subsequently decreased as altitude increased, whereas the
 31 differences in PM₁₀ remained significant below 1.2 km. For PM_{2.5}, the strongest enhancement appeared between 7:00
 32 and 14:00 (Beijing time, BJT). A subtle lifting with height was observed around midday. PM₁₀-polluted days were
 33 characterized by a greater vertical extension of high aerosol extinction (~~reaching~~ up to ~1.2–1.4 km) but a shorter
 34 duration of strong extinction. ~~In contrast, to~~ PM_{2.5}-polluted days, ~~which~~ exhibited a ~~more~~-persistent but vertically
 35 confined aerosol layer. ~~PM₁₀ pollutant tended to accumulate within the altitude range of 0.4–1.2 km on polluted days.~~
 36 The vertical wind shear (VWS) was weaker on PM_{2.5}-polluted days compared to clean days. On PM₁₀-polluted days,
 37 the VWS in the near-surface layer (1000–900 hPa) was significantly stronger than that on clean days, especially
 38 during the early morning and evening periods. The PM_{2.5} pollution in Hefei was mostly contributed by temperature
 39 inversion and high relative humidity, while PM₁₀ pollution was driven by long-range transport of aerosol particles
 40 under the cold front system and dry conditions. These findings ~~reveal~~ ~~highlight~~ ~~the~~ complex interactions between
 41 aerosol optical properties, boundary-layer dynamics, and synoptic ~~scale meteorology conditions~~, providing new
 42 insights into the vertical ~~processes governing~~ air quality ~~processes~~ in eastern China.

43 **Keywords:** Aerosol LiDAR, Vertical profile, Heavy pollution episodes, Vertical wind shear, Fine and coarse
 44 particulate matter.

45 1. Introduction

46 Air pollution remains one of the most pressing environmental challenges globally, with fine particulate matter
 47 and inhalable coarse particles posing serious risks to public health and atmospheric visibility ([Chen et al., 2023](#); [Deng
 48 et al., 2023](#)). Air quality is closely related to the concentration of pollutants suspended in the atmosphere ([Wang et
 49 al., 2024](#)). Solid and liquid phase pollutants, known as aerosols, not only impact air quality and visibility through
 50 multiple mechanisms but also affect the climate by altering Earth's radiation budget and water cycle processes ([Chen
 51 et al., 2016](#); [Miao et al., 2018](#)). In China, substantial improvements in air quality have been achieved in recent years
 52 through stringent emission control policies. However, severe particle pollution events still occur frequently, especially
 53 in winter haze episodes and spring dust storms across the Yangtze River Delta (YRD) region ([Han and Cao 2022](#);
 54 [Wang and Wang 2021](#)). To date, most studies have focused on surface-level air ~~pollution data quality~~, ~~with particular
 55 attention to individual PM_{2.5} and PM₁₀ event in eastern China and urban agglomerations~~ obtained from ground
 56 monitoring networks ([He et al., 2021](#)). These data provide critical insights into near-surface concentrations. However,
 57 they lack information on the vertical distribution and formation mechanisms of pollutants, which is essential for

58 understanding aerosol processes in the troposphere ([Mehta et al., 2021](#); [Mishra and Shibata 2012](#); [Wang et al., 2018](#)).

59 While extensive ground-based monitoring has provided insights into surface-level pollution, the understanding
60 of the vertical distribution and evolution of aerosols remains limited due to a lack of long-term and high-resolution
61 vertical observations ([He et al., 2022](#); [Ou et al., 2021](#); [Shen et al., 2022](#)). The atmospheric boundary layer (ABL)
62 plays a crucial role in regulating aerosol dynamics through physical mechanisms such as turbulence, convection, and
63 mixing ([Gao et al., 2011](#); [Garratt 1994](#); [Tombrou et al., 2007](#)). As the interface between the surface and the free
64 troposphere, the ABL governs the vertical exchange of energy, moisture, and pollutants. Numerous studies have
65 demonstrated that lower ABL heights could trap pollutants near the surface, leading to elevated PM_{2.5} levels. These
66 lower heights are often associated with thermal inversions and stagnant synoptic conditions ([Liu et al., 2020](#); [Sun et
67 al., 2024a](#)). Under such conditions, limited mixing suppresses the vertical dispersion of aerosols, allowing surface
68 emissions to accumulate rapidly, particularly in urban areas with high anthropogenic activity. In contrast, strong
69 vertical mixing and higher ABL heights enhance dispersion and dilution of pollutants, which frequently results in
70 improved surface air quality ([Jin et al., 2021](#)). Moreover, interactions between the lower ABL and the overlying free
71 troposphere, including vertical wind shear, subsidence, and entrainment processes, also significantly influence
72 aerosol layering and transboundary transport ([Deng et al., 2023](#); [Li et al., 2022](#)). These interactions are significant
73 during transition periods such as the morning boundary layer growth phase or evening collapse, which strongly affect
74 aerosol vertical distribution ([Li et al., 2018](#)). Despite these known mechanisms, detailed observations of the vertical
75 structure of aerosols and their relation to meteorological dynamics remain limited under varying pollution conditions
76 and across different seasons ([Yang et al., 2025](#)). Comprehensive long-term observations are still needed to
77 characterize how meteorology influences aerosol stratification and transformation over time.

78 Active remote sensing techniques, such as aerosol Light Detection and Ranging (LiDAR), have emerged as
79 powerful tools to fill this observational gap ([Ansmann et al., 2013](#); [Chen et al., 2024a](#)). Unlike passive satellite-based
80 instruments, LiDAR systems provide high-resolution vertical profiles of aerosol optical properties at fine temporal
81 scales and under both day and night conditions, capable of capturing sub-kilometer vertical gradients and diurnal
82 variability that are critical for understanding boundary-layer dynamics ([Wang et al., 2024](#); [Zhang et al., 2020b](#)). It
83 enables continuous monitoring of aerosol structure, boundary layer formation, and pollutant layering in response to
84 atmospheric dynamics ([Fan et al., 2024](#); [Fang et al., 2024](#); [Li et al., 2024](#)). Specifically, polarization-sensitive aerosol
85 LiDAR can simultaneously retrieve extinction coefficients and depolarization ratios, which serve as indications of
86 aerosol concentration and morphology ([Cairo et al., 2024](#); [Chen et al., 2024a](#); [Kumar et al., 2024](#)). The extinction
87 coefficient quantifies the total attenuation of light caused by scattering and absorption by particles, and it is directly

88 related to aerosol optical depth and visibility ([Chen et al., 2024b](#); [Sun et al., 2024b](#)). The depolarization ratio
89 distinguishes the spherical and non-spherical particles, providing insights into aerosol types such as secondary
90 inorganic aerosols, biomass burning smoke, and desert dust. These parameters are crucial for understanding not only
91 the optical but also the physical properties of aerosols ([Chen et al., 2024b](#); [Gebauer et al., 2024](#)). However, most
92 previous studies using such measurements have been limited to short-term campaigns or case studies of individual
93 pollution episodes ([Chen et al., 2022](#); [Zhong et al., 2018](#)). These attempts often lack the long-term temporal continuity
94 and seasonal representativeness necessary~~spatial and temporal representativeness necessary~~ for climatological or
95 process-level understanding, particularly in regions subject to strong seasonal and meteorological variability.

96 Long-term monitoring of air pollutants is essential for the comprehensive understanding of their temporal
97 characteristics ([Fan et al., 2021](#); [Xiang et al., 2021](#)). Unlike ground-based air quality monitoring networks, vertically
98 resolved data are required to evaluate the entire process of pollution events, vertical mixing, and potential long-range
99 transport ([Wang et al., 2024](#)). Passive satellite remote sensing techniques have proven useful in bridging spatial gaps
100 in air quality data, but are limited in their ability to resolve vertical structures with high temporal accuracy due to
101 their coarse resolution and fixed overpass times ([Chen et al., 2023](#)). Chemical transport models (CTMs) have been
102 widely used to simulate the spatiotemporal behavior of aerosols and their interactions with meteorology ([Wang et al.,](#)
103 [2025](#); [Xiong et al., 2023](#)). However, their accuracy is constrained by uncertainties in emissions inventories, boundary
104 conditions, meteorological input fields, and the representation of aerosol microphysics. In addition, model
105 performance varies significantly by region and pollution type ([Zhan et al., 2024](#)). LiDAR technology provides high
106 temporal resolution and fine vertical resolution measurements~~spatiotemporal resolution vertical measurements~~ of
107 aerosol and meteorological variables, including aerosol extinction, backscattering, and wind profiles ([Chen et al.,](#)
108 [2023](#); [Chouza et al., 2015](#); [Zhang et al., 2020b](#)). This capability makes LiDAR particularly suitable for investigating
109 aerosol evolution and transport within the ABL and lower troposphere. Nonetheless, long-term time series analyses
110 based on continuous LiDAR measurements remain limited in the literature.

111 To address these limitations, we conducted multi-year observations using an aerosol LiDAR system in Hefei.
112 The deployed LiDAR system provides real-time vertical profiles of aerosol extinction and depolarization ratios,
113 allowing for a detailed assessment of aerosol structure under different pollution levels. This study fills the
114 observational gap in the long-term vertical characteristics of both fine and coarse particulate pollution over this region.
115 We characterized the vertical and temporal evolution of aerosol properties and linked them with pollution episodes
116 and boundary-layer processes by integrating LiDAR data with surface PM_{2.5} and PM₁₀ concentrations,
117 meteorological observations, and reanalysis products. Therefore, the objectives of this study were (1) to analyze the

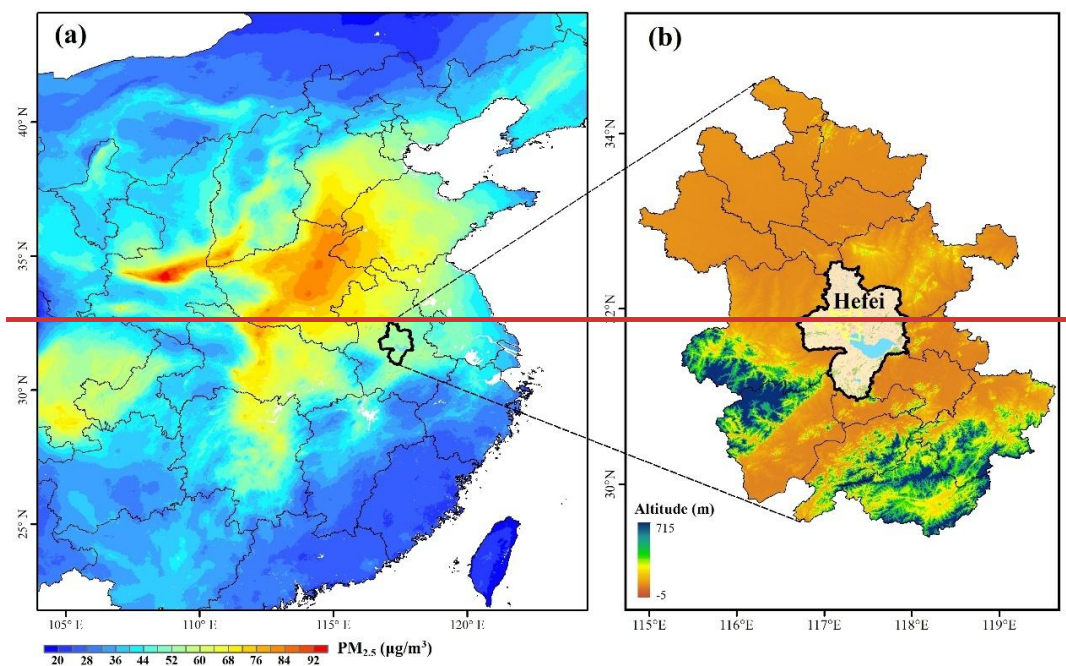
118 seasonal and diurnal variations of vertical profiles with aerosol extinction and depolarization data; (2) to compare the
119 vertical structures on polluted and clean days to clarify the differences in aerosol optical properties between these
120 two conditions; (3) to assess the relationship between aerosol layering and near-surface pollutant concentrations at
121 different heights; and (4) to investigate the spatiotemporal evolution of aerosols during specific pollution episodes
122 and explore the mechanisms of their vertical structure, meteorological conditions, and accumulation process. The
123 findings are expected to enhance our understanding of aerosol vertical structure in eastern China and provide
124 scientific support for air quality management and modeling efforts.

125

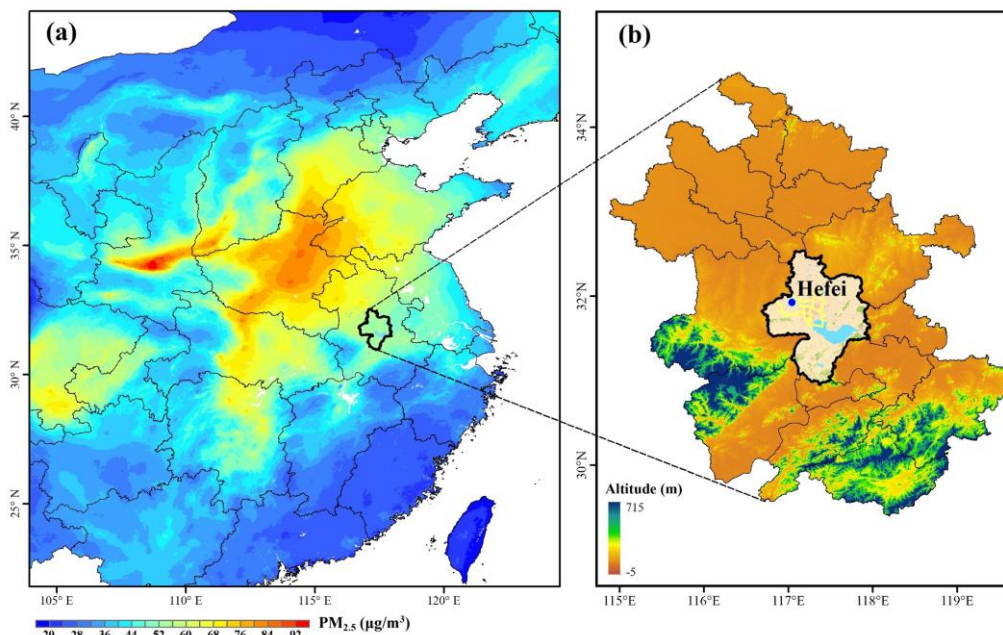
126 **2. Data and methods**

127 **2.1 Study region**

128 Hefei occupies a strategic location, bridging the Beijing-Tianjin-Hebei metropolitan cluster and the Yangtze
129 River Delta economic hub. The study area lies in a transitional climatic zone, where temperature inversions occur
130 frequently in winter. Such conditions often result in stagnant air that limits pollutant dispersion. In addition, the
131 geography of Hefei plays a critical role in exacerbating air quality challenges. Hefei is surrounded by the Dabie
132 Mountains in the west and the Huangshan ranges in the south. The open plains dominate its northern and eastern
133 frontiers (**Fig. 1b**). These natural barriers hinder the southward dispersion of airborne pollutants while trapping those
134 transported from industrialized northern regions within the basin. The unique combination of geographic constraints
135 and atmospheric conditions has made Hefei a focal point for studying complex pollution mechanisms. Researchers
136 here focus particularly on the synergistic effects of regional transportation, local emissions, and meteorological
137 drivers on particulate matter formation ([Fang et al., 2024](#); [Huang et al., 2016](#); [Liu et al., 2024](#)).



138



139

140 **Figure 1.** The spatial distribution of (a) the averaged $PM_{2.5}$ concentration during winter from 2021 to 2023 (Ministry
 141 of Environmental Protection in China, <https://air.cnemc.cn:18007/>) and (b) the location of the study area (Hefei,
 142 China). The digital elevation model (DEM) data are derived from the NASA Shuttle Radar Topography Mission
 143 (SRTM) 30 m product (<https://glovis.usgs.gov/>), and the land use map of the study area is obtained from the 30 m
 144 resolution annual China Land Cover Dataset (CLCD) dataset. The monitoring station is marked by the blue dot.

2.2 Aerosol LiDAR data

The LGJ-05 aerosol LiDAR combines traditional radar technology and modern laser technology ~~with 355 nm,~~ ~~with 532 nm,~~ ~~and 1064 nm~~ as detection light sources. Measurements at 532 nm were utilized exclusively for ~~the present~~this study. The LiDAR emits ~~532 nm~~ a laser pulses into the atmosphere to capture backscattered signals, thereby obtaining key aerosol optical characteristics. As a polarization-sensitive system, it can retrieve extinction coefficients and depolarization ratios to characterize aerosols in the atmosphere. During the transmission process, the laser pulse is scattered and extinguished by atmospheric aerosol particles. The intensity of backscattered light at different altitudes correlates with the scattering and extinction properties of aerosol and cloud particles at those altitudes. The backscattered light from spherical particles can maintain its polarization characteristics of the emitted pulse since the emitted laser pulse is linearly polarized. In contrast, non-spherical particles (such as dust particles and ice crystals in cirrus clouds) depolarize the backscattered light due to their irregular shapes and asymmetric interaction with linearly polarized laser pulses. The LiDAR could detect the echo signals of the parallel and vertical components in the backscattered light, enabling acquisition of the vertical profile of the depolarization ratio of atmospheric aerosol particles. It could enable three-dimensional monitoring of the atmosphere in real time through active remote sensing, with the capacity to invert spatiotemporal distribution information such as aerosol extinction, depolarization, and water vapor mixing ratio in the atmosphere. The aerosol extinction coefficient reflects the attenuation capacity of aerosol particles to incident light, while the depolarization ratio indicates the non-spherical nature of aerosol and cloud particles. A higher extinction coefficient typically indicates a larger concentration of aerosol particles or stronger light-scattering/absorbing properties. However, greater depolarization values denote a higher abundance of non-spherical aerosol particles (e.g., dust, rugged industrial aerosols) or mixed-phase cloud constituents. By contrast, lower depolarization ratios indicate a dominance of spherical particles or simpler particle structures.

~~The LGJ-05 aerosol LiDAR accomplishes all these operations using a laser as the light source. The laser system generates high energy light beams at wavelengths of 532 nm, 355 nm, and 1064 nm. The three wavelength laser beams are emitted into the atmosphere through a broadband mirror and undergo Mie scattering with aerosols.~~ Since the instrument is capable of receiving data below 30 km, the effective detection range of the aerosol LiDAR can cover 0.2-6 km and 0.2-15 km for daytime and nighttime, respectively. It offers a vertical spatial resolution of 7.5 meters and a temporal resolution of 10 minutes. The observations were conducted at the National Meteorological Observation Station in the northwest of Hefei (117.06°N, 31.96°E) from March 2021 to May 2023.

2.3 Ground-based observational data

Hourly concentrations of ~~major air pollutants~~ (PM_{2.5} and PM₁₀) were obtained from ground-based monitoring stations in Hefei, which are operated and maintained by the China National Environmental Monitoring Centre (CNEMC) (Liu et al., 2017). These pollutant data were obtained from professional monitoring instruments, with the LGH-~~01B-01E~~ aerosol mass concentration monitor used for PM₁₀ and the LGH-01B ~~aerosol mass concentration monitor used~~ for PM_{2.5}, both of which apply the beta attenuation method. All instruments are calibrated regularly according to national standards, and the data undergo strict quality control procedures, including hourly, daily, and annual audits, as described in the China Environmental Monitoring Quality Assurance and Quality Control Manual. It should be noted that we focused on PM_{2.5} and PM₁₀ concentrations during ~~the~~ winter and spring ~~seasons~~, respectively. All comparisons between PM_{2.5} and PM₁₀ pollution episodes were conducted across both seasons. The hourly resolution of the dataset allows for capturing diurnal variations in pollutant levels, while the multi-pollutant data facilitates analysis of the differences in meteorological responses of pollutants in Hefei.

The observed meteorological variables were obtained from the China Meteorological Administration (CMA) (<http://data.cma.cn/en>), measured by the Vaisala PTB210 Digital Barometer for atmospheric pressure, the Vaisala HMP155A Temperature and Relative Humidity Probe for air temperature (T) and relative humidity (RH), the EL15-2C Wind Direction Sensor for wind direction (WD), and the EL15-1C Wind Speed Sensor for wind speed (WS). All meteorological instruments are routinely maintained and calibrated to ensure the accuracy and reliability of observational data.

2.4 ECMWF reanalysis data

This study aims to investigate the impact of the synoptic system on PM_{2.5} and PM₁₀ pollution. The ERA5 reanalysis dataset, freely accessible via the Copernicus Climate Change Services platform (<https://cds.climate.copernicus.eu/datasets>), serves as the data source. Vertical atmospheric data within the ERA5 dataset are interpolated to 37 pressure levels. This interpolation yields comprehensive data ranging from the Earth's surface to the upper atmosphere. Given its high spatial and temporal resolution, the ERA5 dataset has been widely employed in extreme weather events, climate prediction, and air pollution studies (Fan et al., 2021; Zhang et al., 2020b).

This study collected hourly geopotential height, vertical wind velocity, temperature, and humidity data. The data correspond to multi-pressure levels (500 hPa, 700 hPa, 725 hPa, 750 hPa, 775 hPa, 800 hPa, 825 hPa, 850 hPa, 875 hPa, 900 hPa, 925 hPa, 950 hPa, 975 hPa, and 1000 hPa) ~~and cover the period from 2021 to 2023.~~ The spatial

205 resolution of our dataset was $0.25^{\circ} \times 0.25^{\circ}$ (zonal and meridional) and supports a detailed and accurate exploration
206 of the synoptic-particulate matter relationship. The data were extracted for winter and spring during 2021–2023,
207 consistent with the periods of the surface pollutant and aerosol LiDAR observations.

209 2.5 Quality control

210 To explore the potential of aerosol LiDAR observations and improve data reliability, this study extracted the
211 extinction coefficient and depolarization ratio data at 532 nm from the LiDAR system for the period from March
212 2021 to May 2023. In the quality control process, specific criteria were established to ensure the reliability of the
213 retrieved parameters. Specifically, it covers three steps for outlier detection, removal of spurious points, and temporal
214 consistency analysis. Outlier detection was conducted to eliminate all records outside the normal value range
215 according to the parameter intervals provided by the instrument, with specific thresholds applied based on the signal-
216 to-noise ratios (SNR) of the parallel (P) and perpendicular (S) channels. The extinction coefficient at 532 nm was
217 calculated using data from the ~~parallel (P)~~ channel, which was considered reliable only when the corresponding
218 ~~signal-to-noise~~ SNR ratio (SNR) exceeded three. The depolarization ratio was derived from the P and ~~perpendicular~~
219 ~~(S)~~ channels, and data were accepted only when both channels had SNRs greater than three. The P channel detects
220 linearly polarized light in the parallel direction, while the S channel detects linearly polarized light in the
221 perpendicular direction. Based on the time series of SNR records, the individual extinction and depolarization data
222 were cross-referenced. Temporal consistency analysis was conducted by identifying records that deviated by more
223 than three standard deviations from the mean as outliers. The original LiDAR data have a 10-minute temporal
224 resolution. After quality control, these data were averaged to hourly resolution to be consistent with the hourly
225 ground-based pollutant observations. To further improve data reliability, this study calculated the credibility ratio of
226 the extinction coefficient and depolarization ratio at different altitudes. Based on the criterion of a 60% valid data
227 availability rate, the effective detection ranges for the 532 nm of the extinction coefficient and depolarization ratio
228 were 0.2025~1.815 km.

230 2.6 Methodology

231 2.6.1 Definition of polluted and clean

232 In this study, the data from 2021-2023 are gathered and categorized into four seasons: spring (Mar.-May),
233 summer (Jun.-Aug.), autumn (Sep.-Nov.), and winter (Dec.-Feb.). Given that PM_{2.5} pollution is most severe in winter
234 and sand-dust events are frequent in spring, the definitions of polluted and clean days in this study primarily focus

235 on these two seasons. Days in winter when the daily average concentration of PM_{2.5} exceeds 75 µg/m³ are defined as
 236 PM_{2.5}-polluted days. Conversely, days in winter with a daily average PM_{2.5} concentration below 50 µg/m³ are
 237 classified as PM_{2.5}-clean days. For PM₁₀, spring days with daily average concentrations above 150 µg/m³ are defined
 238 as polluted days, while those below 100 µg/m³ are considered clean days (Ministry of Environmental Protection of
 239 the People's Republic of China, Technical Regulation on Ambient Air Quality Index, 2012). To eliminate the wet
 240 deposition effect of precipitation, all observations in this study excluded precipitation daily data.

241 2.6.2 Calculation of Vertical Wind Shear

242 The vertical wind shear (VWS) is a crucial factor in characterizing the change in wind velocity with height. It
 243 is defined ~~based on~~as the ~~variation magnitude of wind vector~~the difference in the bulk wind vector across atmospheric
 244 layers between two vertical levels, quantified by the magnitude of the difference between upper and lower
 245 levels normalized by the height difference. The VWS can be calculated using the following formula:

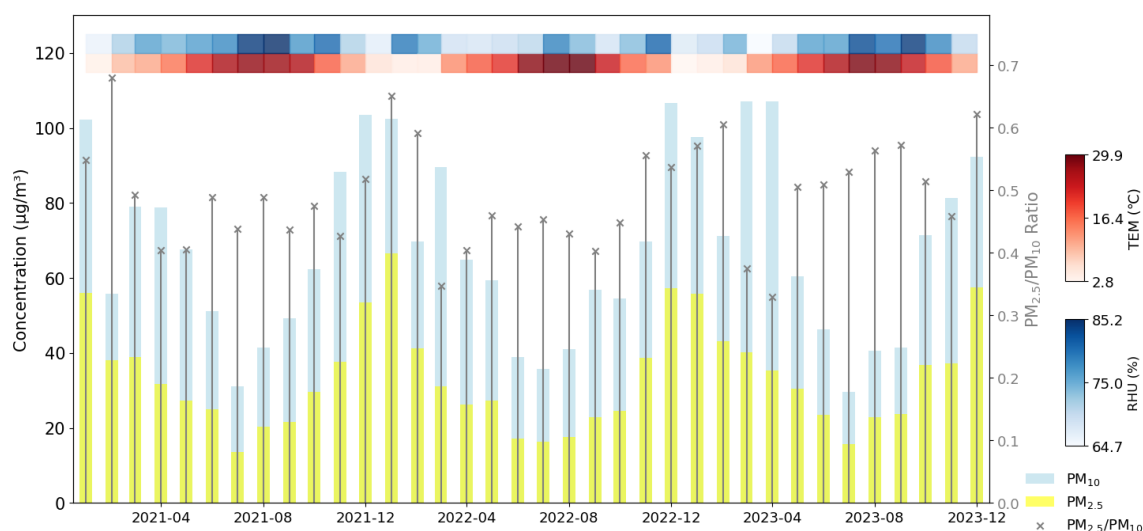
$$245 \text{ VWS} = \frac{\sqrt{(u_t - u_l)^2 + (v_t - v_l)^2}}{(z_t - z_l)} \times 1000 \quad (1)$$

246 Where VWS is measured in units of m/s-km⁻¹. u_t and u_l denote the zonal wind components at the upper z_t and lower
 247 z_l levels, respectively, while v_t and v_l represent the corresponding meridional wind components. This calculation aids
 248 in quantifying the vertical dynamic forces that may impact the dispersion and transportation of pollutants.

250 3. Results and discussion

251 3.1 Variations of inter-annual PM_{2.5} and PM₁₀

252 **Figure 2** shows the variations in the concentrations of PM_{2.5} and PM₁₀ pollutants from 2021 to 2023. Both PM_{2.5}
 253 and PM₁₀ pollutants exhibited a clear seasonal pattern, with concentrations higher in winter and lower in summer
 254 ([Liu et al., 2021](#); [Wang et al., 2024](#)). In addition, PM₁₀ concentrations were relatively high during the spring months
 255 of 2022 and 2023, likely driven by increased dust events such as sand-dust storms that commonly occurred during
 256 this season. High PM_{2.5}/PM₁₀ ratios (≥ 0.5) during winter suggest a dominant contribution from fine particulate
 257 matter, whereas lower ratios (≤ 0.5) in spring indicate an increased presence of coarse particles ([Liu et al., 2015](#)).
 258 The episodic PM₁₀ peaks observed in spring 2022–2023 coincided with a pronounced decrease in the PM_{2.5}/PM₁₀
 259 ratio in Hefei. This phenomenon reflected intensified pollution of coarse-mode aerosols. Although winter months
 260 also suffered elevated PM₁₀ pollution, the concurrent high PM_{2.5} concentrations complicated the separation of dust-
 261 related contributions. In contrast, the lower PM_{2.5}/PM₁₀ ratios in spring facilitated the distinct observation of dust
 262 events due to the reduced interference from fine particulate matter.



263

264 **Figure 2.** Monthly variation of PM_{2.5} (marked as the yellow bars) and PM₁₀ (marked as the blue bars)265 concentrations, PM_{2.5}/PM₁₀ ratio (the grey lines with markers on top), temperature (TEM), and relative humidity

266 (RH) during 2021-2023 in Hefei (Beijing time, BJT = UTC + 8 h).

267

268 The hourly PM_{2.5} and PM₁₀ concentrations exhibited clear diurnal variation on both polluted and clean days (**Fig.**269 **3**). Polluted days showed significantly higher PM_{2.5} levels, with hourly averages ranging from 100 to 125 µg/m³,270 compared to the stable 35–55 µg/m³ range observed on clean days. The PM_{2.5} concentrations on polluted days

271 displayed a bimodal pattern. The concentrations remained consistently high throughout the morning period from

272 04:00 to 11:00 (Beijing time, BJT), with the peak at 10:00–11:00 (BJT) ([Dai et al., 2020](#)). Valleys in PM_{2.5}

273 concentrations occurred at 16:00 (BJT), possibly associated with enhanced atmospheric dispersion from midday

274 heating that facilitates the dilution of particulate matter. Concentrations initiated an upward trend from 17:00 (BJT),

275 with a gradual increase culminating in a peak between 21:00 and 22:00 (BJT). In contrast, clean days exhibited a

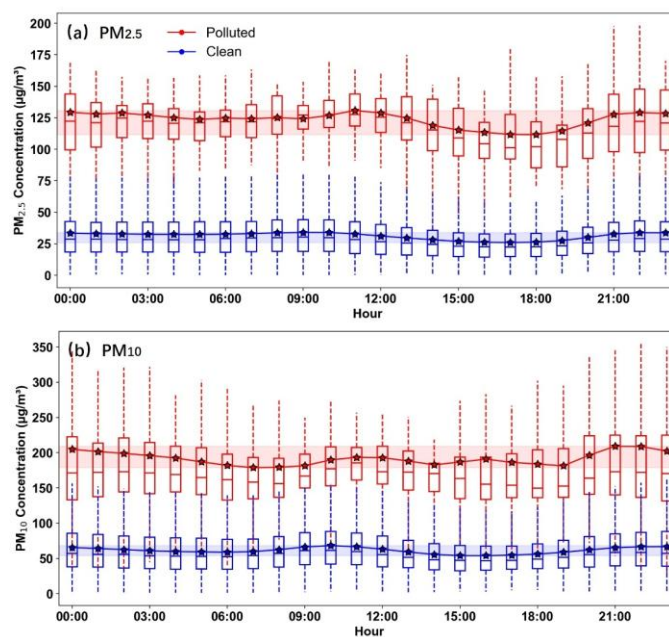
276 subtle morning and overnight peaks. For PM₁₀, polluted days presented pronounced peaks at 10:00–12:00 and 21:00–277 22:00 (BJT), coinciding with increased dust resuspension or construction activities ([Yu et al., 2020](#)). However, valleys

278 occurred at 07:00 and 19:00 (BJT). These may be due to reduced surface disturbances during dawn and enhanced

279 vertical mixing in the afternoon. Clean days maintained relatively low hourly mean PM₁₀ concentrations (50–70280 µg/m³) with minor fluctuations, ~~mirroring the PM_{2.5} pattern~~. The time series curves of pollutants had different peak281 times and amplitudes, indicating distinct origins. PM_{2.5} was more influenced by continuous anthropogenic emissions,282 while PM₁₀ was sensitive to episodic coarse-particle events ([Deng et al., 2023](#); [Wang et al., 2024](#)). These hourly

283 dynamics highlighted the role of diurnal meteorological cycles in modulating particulate matter distribution, with

284 polluted days amplifying both primary emissions and secondary aerosol formation ([Liu et al., 2021](#)).



285

286 **Figure 3.** Hourly mean (a) $PM_{2.5}$ and (b) PM_{10} concentrations on polluted and clean days (Beijing time, BJT = UTC
 287 + 8 h). The blue and red shaded areas represent the ranges of mean concentration values for polluted and clean days,
 288 respectively. The whiskers and boxes represent the 95th, 75th, 50th, 25th, and 5th percentiles, respectively. The stars
 289 represent the mean values of the pollutant concentrations. The solid lines connect the hourly mean values to show
 290 the diurnal variation trends.

291

292 3.2 Temporal variation of vertical distribution structure

293 In addition to the impacts exerted by surface-level pollution, the investigation of vertical distribution is also of
 294 paramount significance for a comprehensive understanding of air quality dynamics. The extinction coefficient at 532
 295 nm shows seasonal and vertical variation. Vertically, extinction coefficients were highest near the surface and
 296 gradually decreased with altitude in all seasons. This vertical decline arises from rapid reductions in aerosol loading
 297 due to vertical mixing, gravitational sedimentation, and dilution with increasing height, as well as the dominance of
 298 weaker molecular scattering above the planetary boundary layer (Wang et al., 2021). Winter presented the highest
 299 extinction values among the four seasons (**Fig. 4a**) (Chen et al., 2023; Wang et al., 2024). This was likely related to
 300 enhanced emissions from domestic heating and stagnant meteorological conditions that restrict vertical mixing
 301 (Zhong et al., 2018). In contrast, summer exhibited the lowest extinction coefficients at 532 nm across the profile,
 302 suggesting the effective dispersion of aerosols due to strong convection and a high planetary boundary layer (Li et
 303 al., 2015). Spring and autumn showed intermediate levels. The most significant differences between seasons appeared
 304 below 1 km, especially in the 0.2–0.6 km range (Zhong et al., 2018). Above 1.0 km, the extinction values in all

305 seasons converged toward high altitude, indicating a reduced aerosol presence in the upper layer ([Liu et al., 2024](#)).

306 The depolarization ratio also exhibited seasonal differences (**Fig. 4b**). With increasing altitude, the contribution
307 of non-spherical particles increases, leading to a steady rise in depolarization ratio. This is attributed to the fact that
308 non-spherical particles exhibit stronger anisotropic light scattering than nearly spherical fine-mode aerosols that
309 dominate near the surface (Wang et al., 2020b). In the lower layer below 0.6 km, spring showed the highest
310 depolarization ratios, which were attributed to a greater proportion of non-spherical particles such as mineral dust or
311 internally mixed soot ([Biuki et al., 2022](#)). This may result from springtime dust resuspension and aged industrial
312 emissions. In contrast, summer had the lowest depolarization ratios, implying that aerosols were dominated by more
313 spherical particles, such as those formed through secondary processes (e.g., sulfate or organic aerosols) ([Sun et al.,](#)
314 [2013](#)). In autumn and winter, values were moderate and stayed between the two extremes. However, the seasonal
315 pattern changed above 0.6 km. Winter showed the highest depolarization ratio, while spring became the lowest. The
316 vertical profile revealed that the change in particle shape with height strongly depends on seasons ([Wang et al., 2004](#)).
317 In winter, the low ambient temperatures in the upper atmosphere promote the formation of non-spherical particles
318 (e.g., ice crystals and irregular aerosols), which substantially enhance the depolarization ratio due to their anisotropic
319 light-scattering properties ([Haarig et al., 2017](#); [Wang et al., 2021](#); [Yu et al., 2021](#)). In addition, elevated aerosol layers
320 were dominated by long-range transported dust with pronounced nonspherical properties. However, aerosols in the
321 upper layer were more spherical and less influenced by dust in spring ([Wang et al., 2020b](#)).

322

323

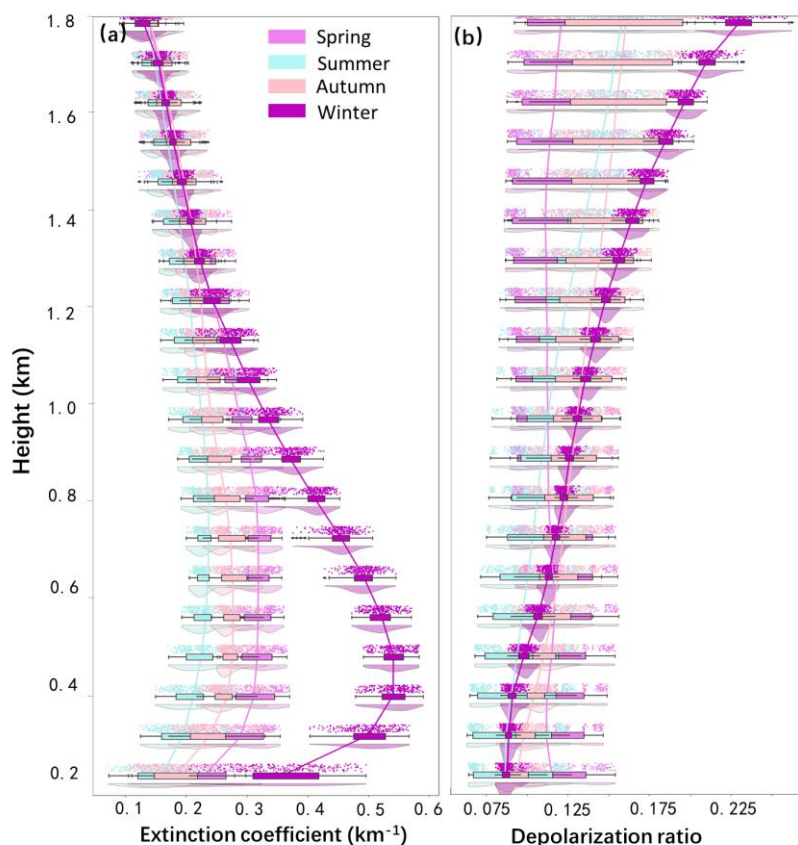


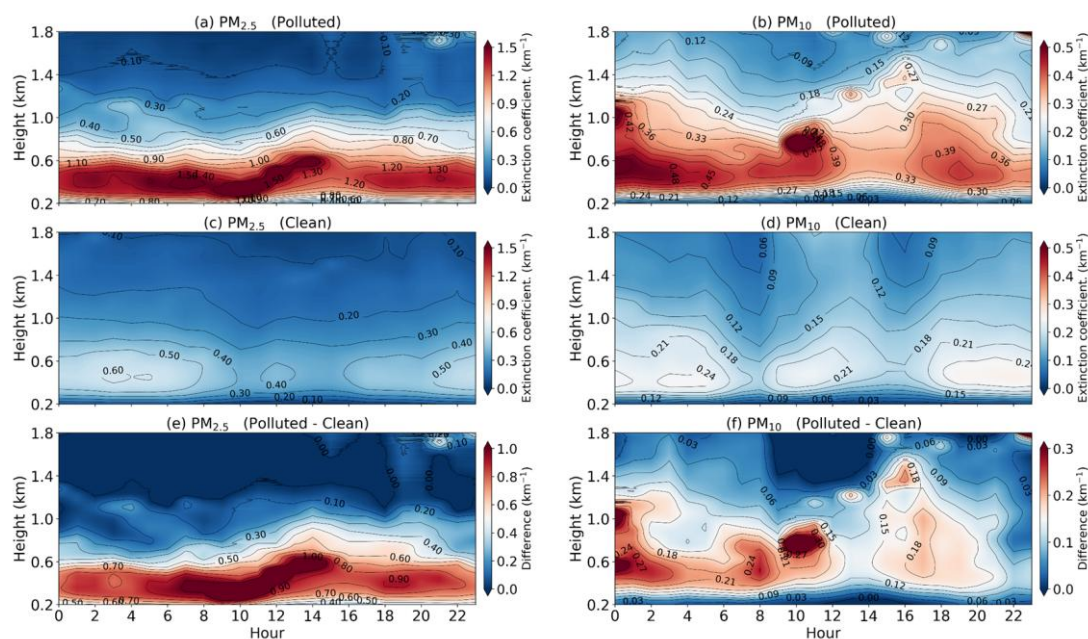
Figure 4. Seasonal variation of vertical aerosol (a) extinction coefficient and (b) depolarization profiles at 532 nm from LiDAR measurements. The whiskers represent the 90th and 10th percentiles, respectively. The shaded areas represent the 25th-75th percentiles. The connected lines depict the trend of mean values across different heights.

The extinction coefficient is significantly higher on PM_{2.5}-polluted days than on PM₁₀ polluted days. This is attributed to the optimal size match between fine-mode particles ($\leq 2.5 \mu\text{m}$) and visible light (0.4–0.7 μm), as well as their chemical components, which are more efficient at scattering and absorbing light (Wang et al., 2021; Chen et al., 2023). The extinction coefficients at 535 nm exhibited clear differences between polluted and clean days for both PM_{2.5} and PM₁₀, with strong vertical and diurnal variation (Fig. 5). For PM_{2.5}, polluted days were characterized by significantly higher extinction values below 0.9 km, especially during the nighttime and the period from early morning to near noon (Wang et al., 2024). This enhancement was mainly attributed to the stable boundary layer and limited vertical mixing during the night, which favored the accumulation of aerosols near the surface. Strong solar radiation enhances photochemical reactions, leading to substantial secondary aerosol formation at noon and a lift in altitude (Fig. 5a). However, extinction values near the surface (below 0.4 km) were relatively low during 12:00-15:00 (BJT), with high values concentrated mainly around 0.6 km. This midday vertical uplift of the aerosol layer corresponds to the decrease in near-surface PM_{2.5} shown in Fig. 3, as enhanced convective mixing lifts fine particles

~~upward and weakens near-surface extinction, which was consistent with the low ground-based PM_{2.5} concentrations during this period shown in Fig. 3. Hence, strong daytime turbulence promotes the vertical transport of aerosols, resulting in an elevated and vertically expanded aerosol layer. The lagged effect of boundary layer development indicated that pollutants accumulated in the morning were not yet fully dispersed (Fig. 5a) (Wang et al., 2024). During this period (12:00–15:00 BJT), the enhanced extinction was concentrated around 0.6 km, extending vertically from the surface to this altitude, rather than peaking near the ground. Extinction values rose not only near the surface but also extended vertically up to around 0.6 km.~~ The upward expansion of aerosols was driven by boundary layer development and persistent emission sources (Dai et al., 2020). In contrast, clean days showed low extinction values throughout the day, with little vertical variation and no significant peak. For PM₁₀, extinction coefficients at 532 nm were also increased on polluted days (Fig. 5b). However, the enhancement of extinction values extended to a higher altitude compared to that of PM_{2.5}, reaching up to 1.2 km. The primary increase occurred during the night and early morning, with a minor secondary rise observed around midday. (Li et al., 2020). Clean-day extinction remained uniformly low with minimal temporal variation (Fig. 5d).

For the depolarization ratio ~~(532 nm)~~, distinct patterns also emerged between polluted and clean days for both PM_{2.5} and PM₁₀ (Fig. 6). For PM_{2.5}, depolarization ratios near the surface (below ~0.6 km) were relatively low on polluted days, particularly during nighttime and early morning (Fig. 6a). This can be attributed to the accumulation of fine, spherical particles in the stable boundary layer, which tend to have lower depolarization ratios. As altitude increased, depolarization ratios rose. This indicates the presence of more irregularly shaped or coarser particles aloft, possibly from transported dust or aged aerosols. In contrast, clean days showed uniformly low depolarization ratios across most heights, consistent with the dominance of fine, spherical aerosols under favorable dispersion conditions (Fig. 6c). For PM₁₀, depolarization ratios at 532 nm on polluted days exhibited a different behavior (Fig. 6b). Starting around 8:00 (BJT), elevated depolarization values were observed across a broad vertical layer, extending up to ~1.2 km throughout the day. This suggests that coarser particles, which typically have higher depolarization ratios, were more effectively mixed vertically and persisted at higher altitudes compared to PM_{2.5}. The broader vertical distribution of PM₁₀ depolarization signals reflects the larger size and potentially different sources (e.g., resuspended dust, industrial emissions) of these particles, which are less confined by boundary layer dynamics than finer PM_{2.5}. The increased depolarization ratio at noon during PM₁₀-polluted days is attributed to midday boundary layer growth and frontal dust transport, elevating non-spherical coarse particle concentrations. ~~The broader vertical distribution of PM₁₀ depolarization signals reflects the larger size and potentially different sources (e.g., resuspended dust, industrial emissions) of these particles, which are less confined by boundary layer dynamics than finer PM_{2.5}.~~

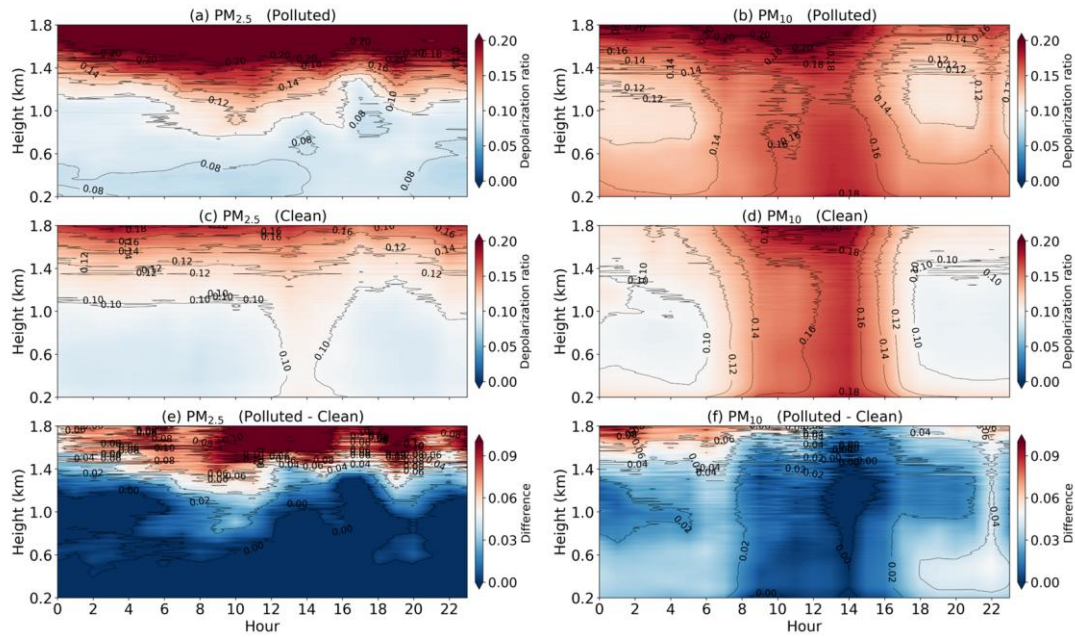
371 The difference between polluted and clean days highlighted a strong increase in near-surface extinction during
 372 early morning on polluted days, indicating suppressed vertical mixing and increased emission accumulation (**Fig.**
 373 **5e&f**). For $PM_{2.5}$, the differences were concentrated near the ground, especially below 0.9 km. The strongest
 374 enhancement appeared between 7:00 and 14:00 (BJT). A subtle lifting with height was observed around midday.
 375 Noon solar radiation maximizes surface heating, which causes severe thermal convection. The lower atmosphere
 376 becomes unstable as a result of the hot Earth transferring energy upward. It could break the stable stratification and
 377 drive upward air motion. Pollutants trapped near the surface are lifted, reducing extinction in the lower layer (<0.4
 378 km) while increasing it aloft as vertical mixing intensifies ([Wang et al., 2024](#)). For PM_{10} , the enhancement tended to
 379 be localized and less vertically extended. The coarse particles may be lifted in upstream source regions, but their
 380 vertical transport weakens significantly along the trajectory. As a result, the transport altitude of PM_{10} reaching Hefei
 381 was largely confined below 1.2 km ([Shim et al., 2022](#)). Compared to $PM_{2.5}$, the high-value region for PM_{10} on polluted
 382 days has a higher vertical extension, and the period of strong extinction is shorter. The particles of PM_{10} are relatively
 383 large and heavy, which leads to rapid sedimentation and thus a short duration of heavy pollution. Pollutants tend to
 384 accumulate in the middle and low altitudes (0.4-1.2 km) on polluted days.



385

386 **Figure 5.** Diurnal variation in the vertical distribution of aerosol extinction coefficient (Winter days for $PM_{2.5}$: First
 387 column; Spring days for PM_{10} : Second column) under days with (a, b) polluted, (c, d) clean, and (Ee, Ff) the
 388 difference between the two. All data are presented in Beijing time (BJT = UTC + 8 h) for the 532 nm channel.

389



390

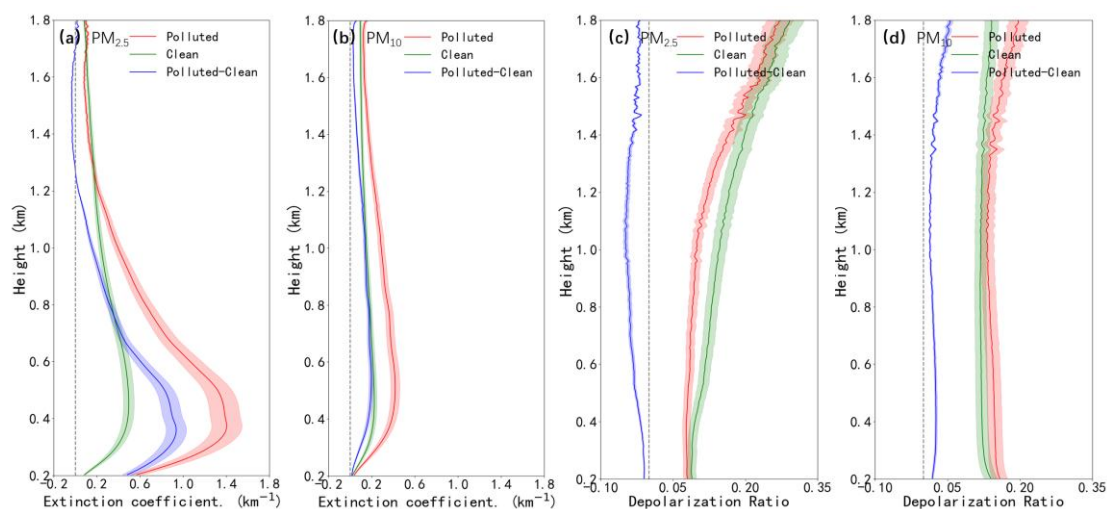
391 **Figure 6.** Same as Fig. 5, but for depolarization ratio.

392

393 To further analyze the vertical aerosol properties under different pollution levels, the mean extinction coefficient
 394 and depolarization ratio at 532 nm were calculated across three representative conditions (**Fig. 7**). Unlike the temporal
 395 variation that emphasized vertical profile distributions (**Fig. 5&6**), these curves highlight altitude-related trends (e.g.,
 396 gradual changes, peak positions, and inflection points) for the comparison between polluted, clean, and difference
 397 conditions. For $PM_{2.5}$, the extinction coefficient decreased exponentially with height and intensified sharply below
 398 0.4 km on polluted days (**Fig. 7a**) ([Wang et al., 2020a](#)). The near-surface value reached up to 1.4 km^{-1} at 0.4 km,
 399 which was nearly three times higher than that on clean days. The difference was most significant within the boundary
 400 layer, especially between 0.3-0.6 km. For PM_{10} (**Fig. 7b**), although the overall extinction values were lower than
 401 those of $PM_{2.5}$, the difference between polluted and clean days remained obvious. The polluted-clean difference for
 402 PM_{10} was more confined below 1.2 km. This discrepancy may be attributed to that the coarse-mode particles tend to
 403 concentrate closer to the surface due to their limited vertical transport.

404 The vertical distributions of the depolarization ratio under different pollution levels are presented in **Figs. 7**
 405 **(c&d)** for $PM_{2.5}$ and PM_{10} , respectively. For $PM_{2.5}$, the depolarization ratio on clean days was higher than that on
 406 polluted days across the entire vertical column up to 1.8 km (**Fig. 7c**). The depolarization ratio of $PM_{2.5}$ increases
 407 with height. The most significant difference in depolarization ratios between polluted and clean days was observed
 408 around 1 km. Above this height, the difference narrowed but clean days still showed slightly higher values. Unlike
 409 near-surface $PM_{2.5}$, which is dominated by local pollution sources, $PM_{2.5}$ at higher altitudes is mainly associated with

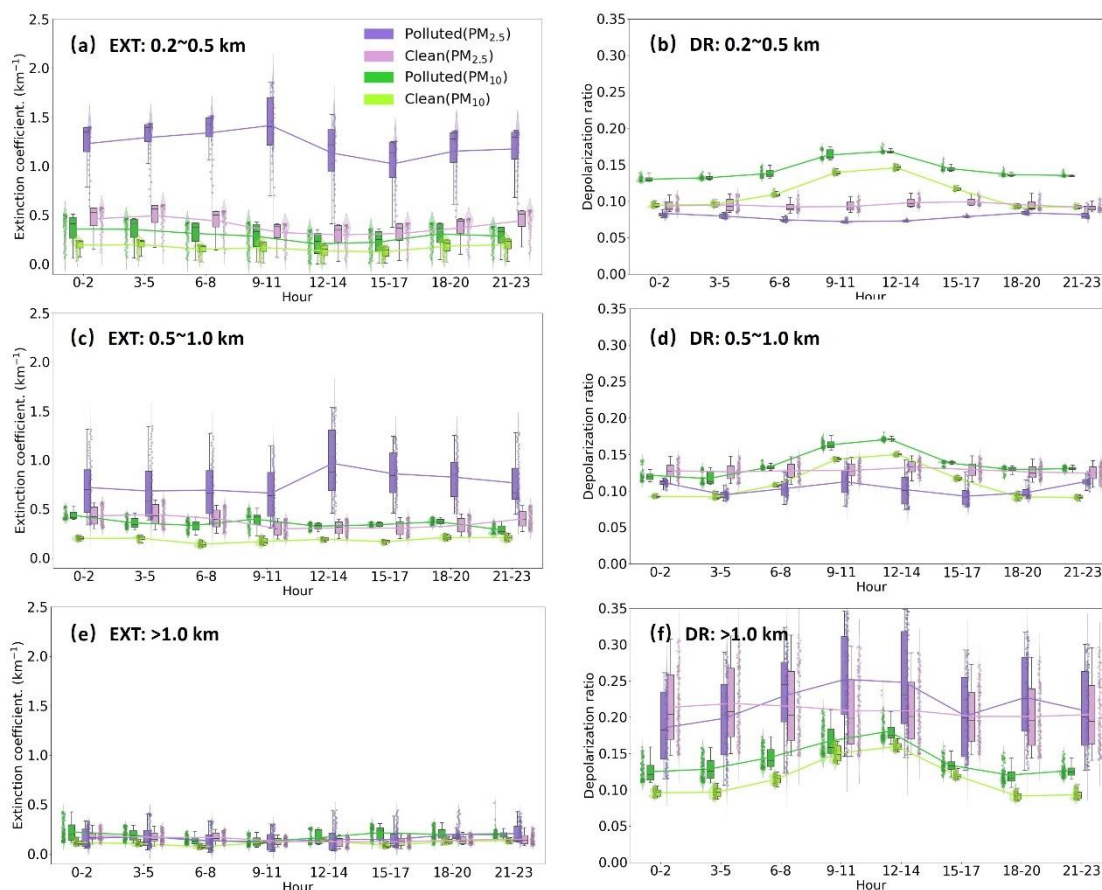
410 long-range transport in the free troposphere, leading to higher depolarization ratios. Higher altitudes have more PM_{2.5}
 411 particles from long-range transport in the free troposphere, which possess higher depolarization ratios (Vakkari et al.,
 412 2021; Wang et al., 2021). Even at higher altitudes, the residual influence of cleaner, non-spherical particle sources in
 413 the background air kept the clean-day depolarization ratio higher (Li et al., 2020). For PM₁₀, the depolarization ratio
 414 of polluted days was higher than that of clean days across the entire vertical range (Fig. 7d), reflecting a greater
 415 abundance of coarse-mode and irregularly shaped particles on polluted days. Below 1.2 km, the depolarization ratio
 416 of PM₁₀ was distinctly higher than that of PM_{2.5} on polluted days. This difference emphasized the dominant influence
 417 of coarse, non-spherical particles (e.g., dust and mechanically suspended material) in the PM₁₀ fraction, particularly
 418 near the surface (Shim et al., 2022). On PM₁₀-polluted days in autumn, the depolarization ratio increased with height,
 419 which is mainly also affected by the long-distance transport of dust in the free troposphere.
 420



421
 422 **Figure 7.** Vertical profiles of aerosol (a, b) extinction coefficient and (c, d) depolarization ratio at 532 nm for (a, c)
 423 PM_{2.5} in winter and (b, d) PM₁₀ in spring on polluted, clean days, and the difference between the two. The gray
 424 dashed line represents the zero line. Note: The extinction coefficient and depolarization ratio of individual polluted
 425 and clean days are positive physical quantities. Negative values in the "Polluted-Clean" panels indicate that the
 426 aerosol optical parameters (extinction coefficient or depolarization ratio) are higher on clean days than on polluted
 427 days. All data are presented in Beijing time (BJT = UTC + 8 h) for the 532 nm channel.
 428

429 **Figure 8** presents the 3-hourly variation of extinction coefficient and depolarization ratio at 532 nm on polluted
 430 and clean days across three altitude layers (0-0.5 km, 0.5-1 km, and 1-1.8 km). Below 0.5 km, the extinction
 431 coefficients were markedly higher on polluted days for PM_{2.5} than that on clean days, with peak values occurring at
 432 03:00-12:00 (BJT) (Fig. 8a), which was consistent with the variation in surface pollutant concentrations (Fig. 3). The

433 depolarization ratio for $PM_{2.5}$ was lower on polluted days in contrast with clean days. This is due to the dominance
434 of spherical fine particles (e.g., sulfates, organic aerosols) from anthropogenic and secondary sources (**Fig. 8a&c**).
435 These particles scatter light less directionally compared to the irregular coarse particles (e.g., dust) prevalent on clean
436 days. In contrast, both the extinction coefficient and depolarization ratio for PM_{10} were high on polluted days ([Zhang
437 et al., 2020a](#)). At the layer between 0.5 and 1 km, the extinction coefficient for $PM_{2.5}$ showed a significant peak
438 around 12:00 to 15:00 (BJT) on polluted days, which was consistent with the upward transport of pollutants to around
439 0.6 km during the same period as shown in the diurnal vertical structure (**Fig. 5**). The extinction values decreased
440 significantly and ~~remained at low levels~~~~showed limited diurnal variability~~ above 1 km (**Fig. 8e**). However, the
441 depolarization ratio remained relatively high during polluted periods. The depolarization ratio for on days in winter
442 was higher than that of spring, mainly because $PM_{2.5}$ pollution contains a higher proportion of irregular particles from
443 coal-fired fly ash and industrial emissions (**Fig. 8f**). The low temperatures inhibit the diffusion and settlement of
444 coarse particles. In contrast, days in spring for PM_{10} pollution were more affected by coarse particles such as
445 windblown dust. Although these particles are irregular in shape, their large particle size makes them prone to settling.
446 Moreover, the strong atmospheric fluidity in spring led to a slightly lower depolarization ratio compared to winter.
447 Overall, the greatest contrast between polluted and clean days was observed in the lowest layer, where both particle
448 concentration and shape varied most distinctly with pollution level and time of day ([Zhong et al., 2018](#)).
449



450

451 **Figure 8.** Diurnal variations of (EXT: a, c, e) extinction coefficient and (DR: b, d, f) depolarization ratio at 532 nm
 452 on polluted and clean days for PM_{2.5} and PM₁₀ at (a, b) 0.2-0.5 km, (c, d) 0.5-1.0km, and (e, f) above 1.0 km,
 453 respectively. The whiskers represent the 90th and 10th percentiles, respectively. The shaded areas represent the 25th-
 454 75th percentiles. The connected lines depict the trend of mean values across different heights. All data are presented
 455 in Beijing time (BJT = UTC + 8 h) for the 532 nm channel.

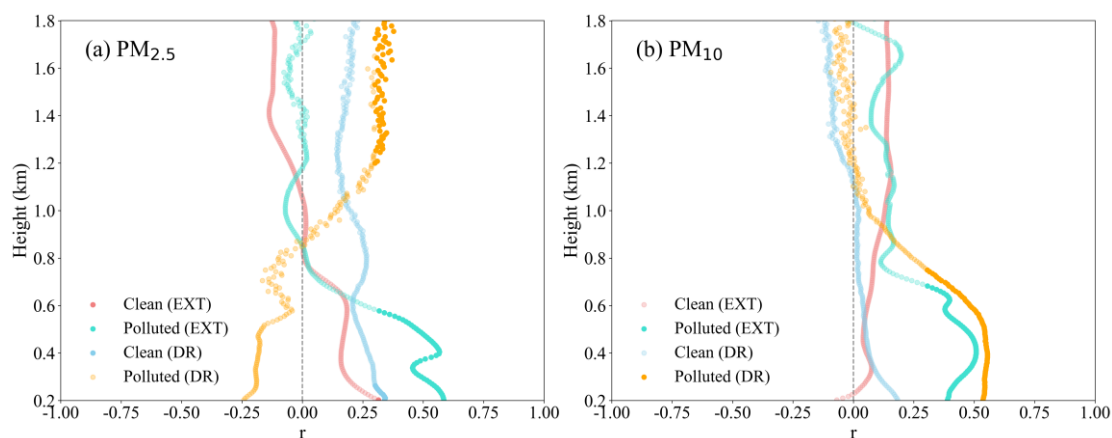
456

457 3.3 Role of aerosol extinction coefficient and depolarization ratio at different altitudes on 458 ground-based PM_{2.5} and PM₁₀ concentrations

459 **Figure 9** shows the vertical profiles of the relationships between surface pollutant concentrations and aerosol
 460 optical properties (extinction coefficient and depolarization ratio at 532 nm) on polluted and clean days. For PM_{2.5},
 461 the extinction coefficients showed a clear positive correlation with surface PM_{2.5} concentration throughout the profile
 462 below 0.9 km on polluted days, marking a key boundary for vertical variation in particle composition (**Fig. 9a**). The
 463 values on polluted days increase sharply near the surface, suggesting a local accumulation. A negative correlation
 464 was observed between the depolarization ratio and PM_{2.5} concentration below 0.9 km on polluted days, as elevated
 465 PM_{2.5} levels corresponded to a higher fraction of fine, spherical particles with low depolarization ~~On polluted days~~

466 ~~with PM_{2.5}, the depolarization ratio was negatively correlated with PM_{2.5} concentration below 0.9 km, with fine~~
 467 ~~particulate matter dominating. As the proportion of fine particulate matter increased, the proportion of spherical~~
 468 ~~particles rose, leading to reduced depolarization~~ (Zhang et al., 2020a). In contrast, clean days showed a consistently
 469 positive correlation between depolarization ratio and surface pollutants throughout the vertical profile.

470 The increased depolarization levels are linked to greater proportions of non-spherical particles, such as dust or
 471 mechanically suspended matter (Vakkari et al., 2021). The depolarization ratio showed consistently positive
 472 correlations with surface PM₁₀ concentration on polluted days, especially below 1.2 km (Fig. 9b). On clean days, the
 473 correlation between the depolarization ratio and PM₁₀ concentration remained near zero, reinforcing that the
 474 depolarization ratio is a distinguishing feature of coarse-mode aerosols. These results revealed the contrasting aerosol
 475 properties between PM_{2.5} and PM₁₀ pollution. PM_{2.5} events were dominated by fine, spherical particles that reduce
 476 depolarization, while PM₁₀ events were closely associated with the presence of coarse, non-spherical particles that
 477 enhanced depolarization signals (Biuki et al., 2022).



479
 480 **Figure 9.** Vertical distributions of correlation (r) between aerosol optical properties (532 nm) and ground-based
 481 pollutants (a: PM_{2.5} in winter, b: PM₁₀ in spring) on clean and polluted days. EXT = extinction coefficient; DR =
 482 depolarization ratio. The gray dashed line represents the zero line.

484 3.4 Analysis of LiDAR observations during heavy pollution episodes

485 Temporal variations of the extinction coefficient and depolarization ratio at 532 nm exhibited a clear association
 486 with PM_{2.5} and PM₁₀ concentrations, effectively highlighting severe pollution periods (Fig. 10). Severe PM_{2.5}
 487 pollution was evident at 10:00 a.m. on January 2, 2023 (BJT), with the maximum hourly concentration reaching
 488 159.6 $\mu\text{g}/\text{m}^3$. The peak of the extinction coefficient matched the actual maximum concentration of PM_{2.5}, with fine
 489 particulate matter exhibiting strong light-scattering properties at this time (Fig. 10a). However, the depolarization

490 ratio of PM_{2.5}-polluted days ~~showed reduced values~~ was markedly decreased during this peak period (**Fig. 10c**).

491 Physically, the extinction coefficient scales with aerosol concentration and size, while the depolarization ratio is

492 governed by particle morphology. Spherical fine particles such as hygroscopic sulfates and nitrates dominating this

493 PM_{2.5} event, leading to increased extinction and decreased depolarization. A dramatic peak in PM₁₀ concentration

494 was observed, with the highest hourly value of 1440 $\mu\text{g}/\text{m}^3$ recorded at 22:00 p.m. (BJT) on April 11, 2023. The

495 severe PM₁₀ event was reflected by a pronounced increase in the extinction coefficient (**Fig. 10b**) ([Sun et al., 2013](#)).

496 In addition, the depolarization ratio exhibited high values during this period, which aligned with the elevated

497 extinction coefficient and was consistent with the irregular morphology of coarse particles that contributed to both

498 stronger light scattering and greater depolarization (**Fig. 10d**). Overall, the profiles of the extinction coefficient and

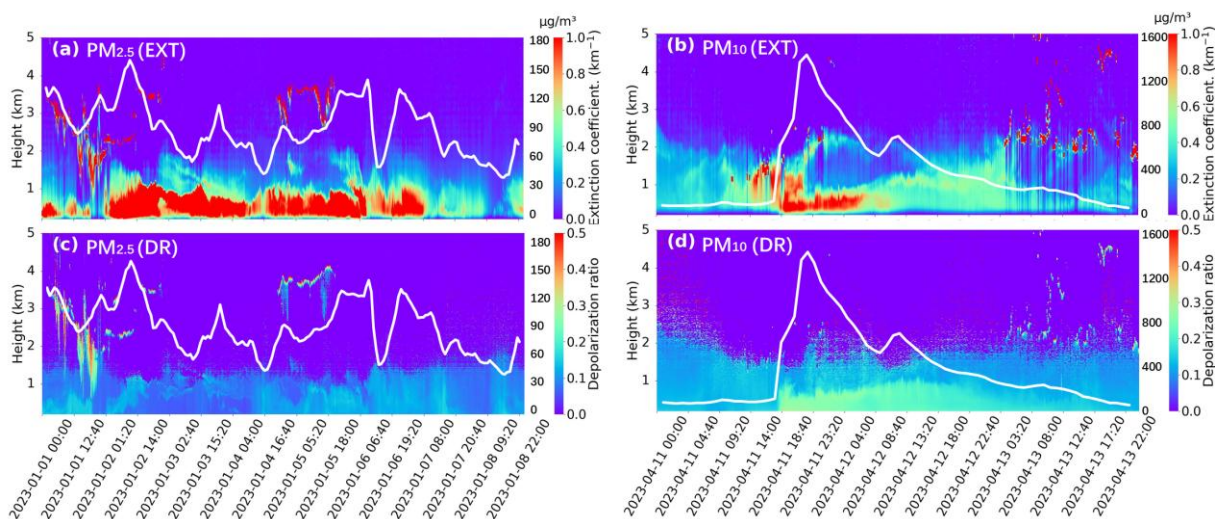
499 depolarization ratio correspond directly to the temporal patterns of PM_{2.5} (January 1–8, 2023) and PM₁₀ (April 11–

500 13, 2023) concentrations (**Fig. 10**). Peaks in pollutant concentrations were reflected in enhanced extinction

501 coefficients and characteristic depolarization ratio patterns ([Zhong et al., 2018](#)). This confirms that these optical

502 metrics effectively identify severe pollution episodes.

503



504 **Figure 10.** Pollution Episodes: Temporal dynamics of (a, b) extinction and (c, d) depolarization parameters for the

505 532 nm channel during severe (a, c) PM_{2.5} (January 1–8, 2023) and (b, d) PM₁₀ (April 11–13, 2023) periods in Hefei.

506 The white lines represent the hourly (a) PM_{2.5} and (b) PM₁₀ concentrations, with their scale on the secondary y-axis.

507 All data are presented in Beijing time (BJT = UTC + 8 h). EXT = extinction coefficient; DR = depolarization ratio.

508

509

510 3.5 Analysis of meteorological conditions and their driving role in air pollution

511 **Figure S1** shows boxplots of the concentrations of PM_{2.5} and PM₁₀ in temperature (T), relative humidity (RH),

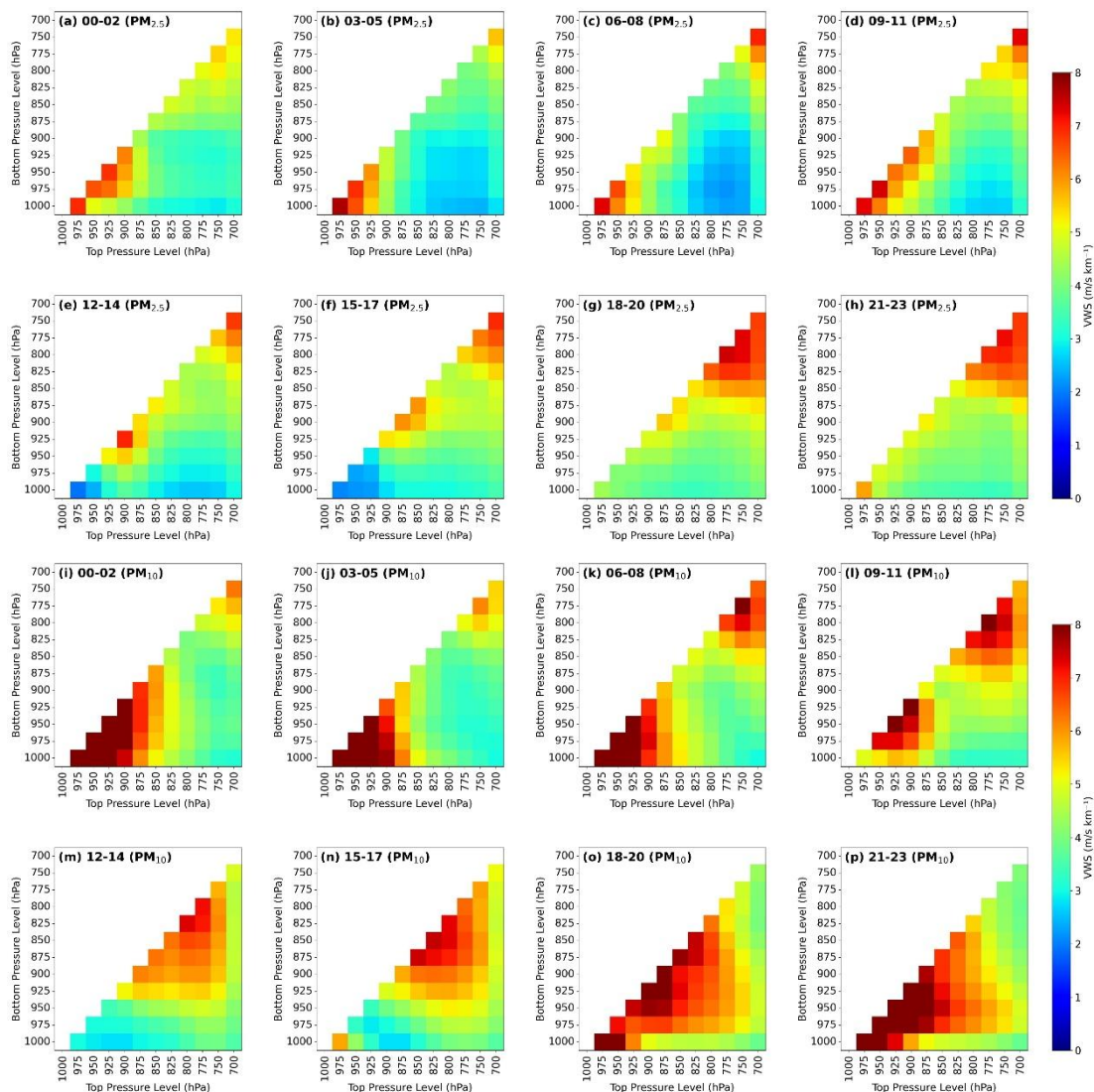
512 surface pressure (PRS), and wind speed (WS) bins, respectively. Overall, the relationships of temperature with PM_{2.5},

513 PM₁₀ were not significant (**Fig. S1a&e**). The RH exerted distinct influences on PM₁₀ and PM_{2.5} concentrations (**Fig.**
 514 **S1b&f**). Higher PM_{2.5} concentrations were associated with increased RH, primarily due to elevated humidity
 515 promoting the condensation of gaseous precursors (e.g., sulfur dioxide, nitrogen oxides) onto pre-existing PM_{2.5}
 516 particles (**Fig. S1b**) ([Wang et al., 2004](#)). Additionally, it accelerated secondary aerosol formation via aqueous-phase
 517 chemical reactions in the atmosphere, thereby elevating PM_{2.5} levels ([Yang et al., 2022](#)). In contrast to PM_{2.5}, the
 518 relationship between PM₁₀ concentrations and RH was inverse (**Fig. S1f**). Higher RH ~~promotes drives coarse particles~~
 519 ~~like PM₁₀ to absorb~~ moisture uptake and growth of coarse PM₁₀ particles, accelerating their sedimentation and wet
 520 deposition, thereby reducing ambient concentrations~~grow in size, and then settle out of the atmosphere more easily.~~
 521 ~~It may also enhance wet deposition processes such as rain or fog scavenging, reducing their airborne concentrations~~
 522 ([Gao et al., 2020](#); [Ma et al., 2023](#)). PRS tended to increase with rising concentrations of PM_{2.5} and PM₁₀ (**Fig. S1c&g**).
 523 The average pressure values were lower on clean days (PM_{2.5} ≤ 75 $\mu\text{g}/\text{m}^3$, PM₁₀ ≤ 150 $\mu\text{g}/\text{m}^3$) and became higher on
 524 polluted days. The high-pressure systems promote atmospheric stability and suppress vertical mixing, thereby
 525 facilitating the accumulation of particulate matter near the surface ([Li et al., 2015](#)). Wind speed exhibited a decreasing
 526 trend with increasing PM_{2.5} concentrations (**Fig. S1d&h**). Lower wind speeds during heavy pollution periods indicate
 527 weak horizontal dispersion, which contributes to the persistence and accumulation of fine particles in the boundary
 528 layer. In addition, the polar plot of PM_{2.5} concentrations shows a directional pattern, with the highest values
 529 predominantly associated with winds from the northwest (**Fig. S2a**). The cities of northern Anhui Province, Henan
 530 Province, and even further north were characterized by dense industrial activities and frequent wintertime heating
 531 emissions, which contribute to elevated PM_{2.5} levels ([Qian et al., 2024](#); [Shi et al., 2018](#)). For PM₁₀, the concentration
 532 distribution was more spatially confined but still shows a dominant contribution from the northwest area ([Huang et](#)
 533 [al., 2016](#)). The most intense PM₁₀ concentrations were clustered in the northwest, appearing localized and patchy
 534 (**Fig. S2b**). ~~This may reflect the influence of transport and mechanical resuspension processes, such as road dust and~~
 535 ~~construction activities.~~

536 VWS is a key dynamic factor affecting pollutant dispersion, as it influences mechanical turbulence and vertical
 537 mixing within the boundary layer ([Deng et al., 2023](#)). **Figures 11** and **12** illustrate the diurnal variation of VWS on
 538 polluted and clean days, respectively. For PM_{2.5}, weak shear persisted throughout the boundary layer on polluted days
 539 when temperature inversions and stable stratification typically dominate the lower atmosphere (**Fig. 11a-h**). Clean
 540 days showed stronger shear during most periods, enhancing upward transport and dilution of fine particles (**Fig. 12**).
 541 Notably, the difference in VWS between polluted and clean days ~~was was~~ more pronounced in the lower boundary
 542 layer (1000–900 hPa) than in the upper boundary layer (875–700 hPa) ([Zhang et al., 2020b](#)). Hence, suppressed

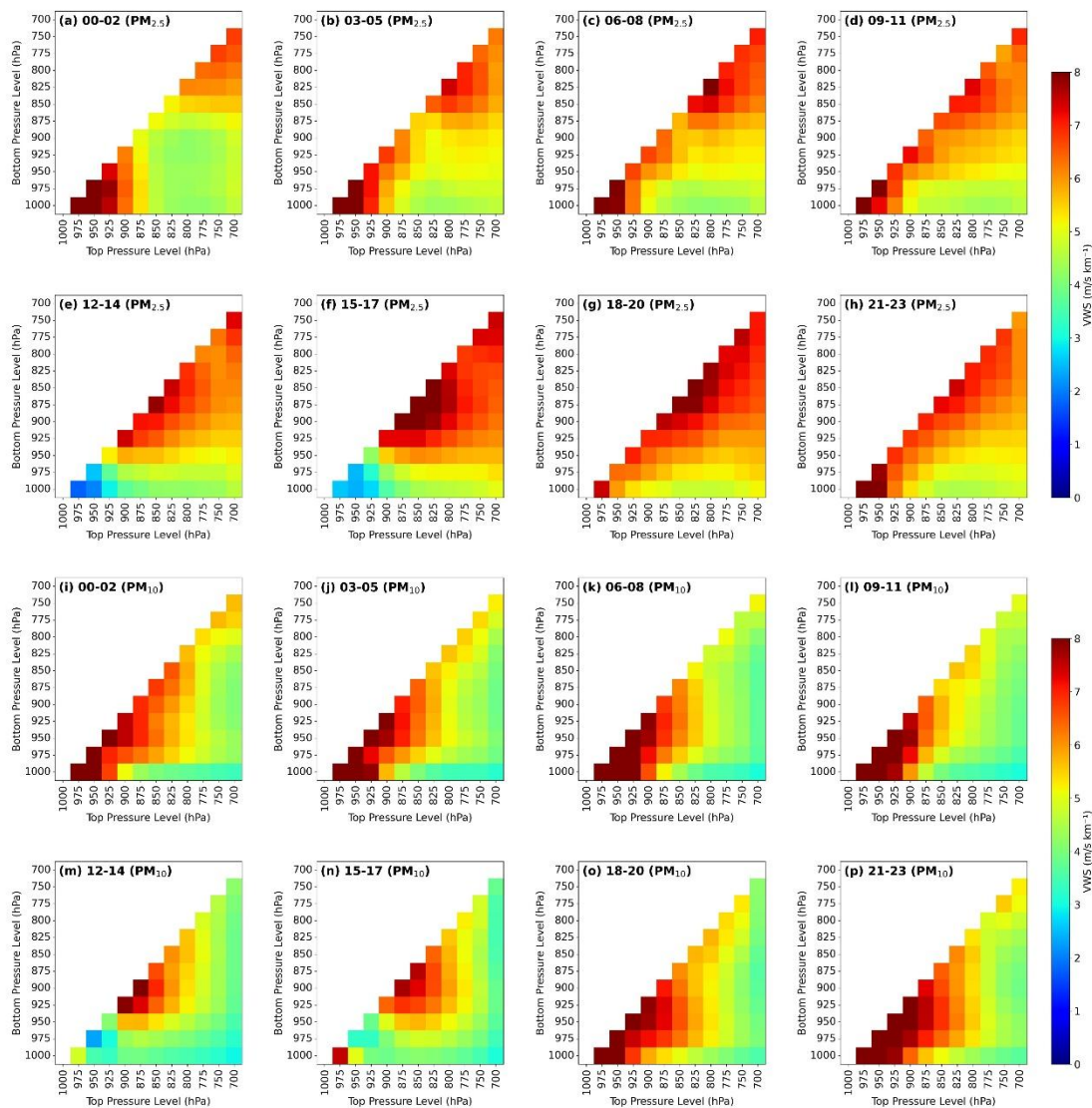
543 vertical mixing near the surface contributed significantly to the accumulation of PM_{2.5}. Surface air quality tends to
544 deteriorate significantly due to pollutant accumulation near the ground, especially in cases where shear is insufficient
545 in the lower layer ([Wang et al., 2024](#)), which was consistent with the trend that the extinction coefficient at 532 nm
546 near the surface is higher than that in the upper layer (**Figs. 7 & 8**).

547 Contrary to the expectation that polluted days generally exhibited weak VWS, the VWS associated with PM₁₀
548 on polluted days was not consistently lower than that on clean days (**Fig. 11 i-p, Fig. 12 i-p**). In particular, dust storms
549 with high PM₁₀ levels are typically accompanied by intensified VWS, which is conducive to dust uplift and transport
550 under dynamic atmospheric conditions ([Yang et al., 2019](#)). The large VWS associated with PM₁₀ would clear the air
551 in the upper air at the beginning but later contributed to raising surface PM₁₀ levels through regional transport at the
552 near-surface and through downward transport of aerosol particles from the upper air. During the onset phase of dust
553 intrusion, intensified shear facilitates both horizontal and vertical transport of dust particles ([Biuki et al., 2022](#)). From
554 00:00 am to 11:00 (BJT), the VWS in the upper layer (850 hPa-700 hPa) gradually increases on PM_{2.5}-polluted
555 days. At night, the near-surface air cools, forming a stable temperature inversion layer that inhibits vertical mixing.
556 Hence, the stable structure would lead to weak VWS in the upper layer. As the sun rises in the mornings, the inversion
557 layer gradually dissipates, and vertical mixing shifts from being suppressed to active (**Fig. 11 i-l**). The VWS in the
558 upper layer gradually increases due to the mixing effect. In addition, PM₁₀ pollution often occurs during cold front
559 passage. The vertical gradient of wind direction and speed changes suddenly near the frontal surface when cold and
560 warm air masses converge. Once the front is located in a certain pressure range, the wind shear may be significantly
561 higher than that in the surrounding layers. The weaker VWS between adjacent pressure layers (e.g., near 825–850
562 hPa) may correspond to the fault distribution (**Fig. 11 i-l**). The sinking of cold air also leads to an increase in VWS
563 at the lower level.



564

565 **Figure 11.** Three-hourly variation of vertical wind shear for (a-h) $PM_{2.5}$ and (i-p) PM_{10} on polluted days in Hefei,
 566 presented as 3-hourly intervals (at (a&i-) 00:00–02:00 BJT, (b&j-) 03:00–05:00 BJT, (c&k-) 06:00–08:00 BJT,
 567 (d&l-) 09:00–11:00 BJT, (e&m-) 12:00–14:00 BJT, (f&n-) 15:00–17:00 BJT, (g&o-) 18:00–20:00 BJT, and (h&p-) 21:00–23:00 BJT). Beijing Time (BJT) is UTC+8, the local standard time used in this study. The axes indicate the
 568 vertical bounds (upper and lower pressure levels) used to compute VWS, where the main diagonal (from top-right to
 569 bottom-left) corresponds to self-referential values for single-layer calculations. The color gradient represents the
 570 magnitude of VWS between adjacent atmospheric layers.
 571



572

573 **Figure 12.** Same as Fig. 11, but under clean days.

574

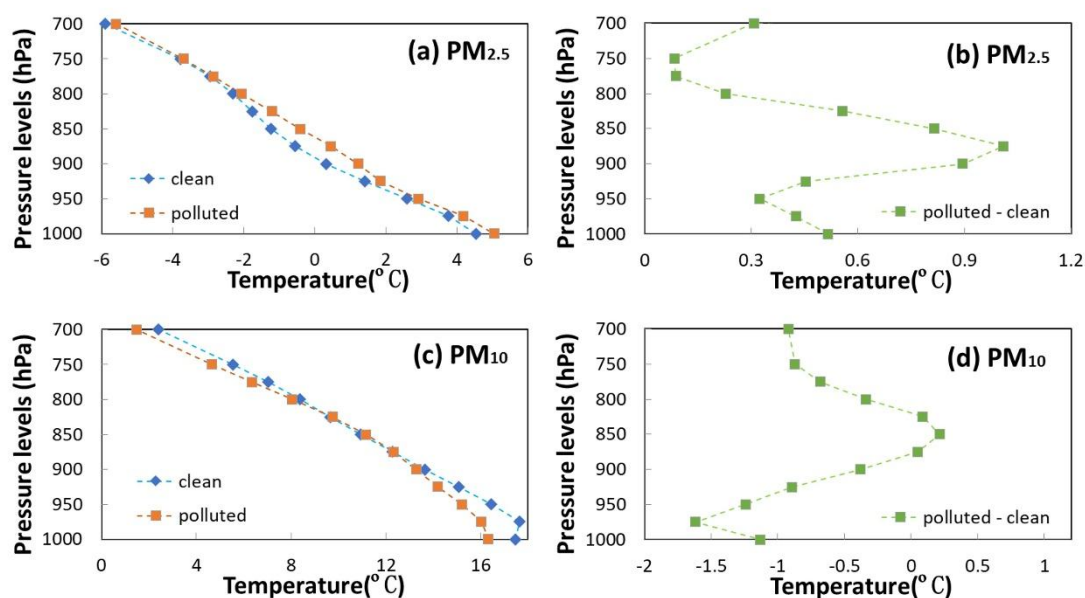
575 To clarify the synoptic influences on $PM_{2.5}$ and PM_{10} pollution, we analyzed the distributions of air temperature
 576 across different pressure levels from March 2021 to May 2023. During $PM_{2.5}$ pollution days, temperatures at all levels
 577 were consistently higher than those on clean days. The warming showed a notable pattern, with the most pronounced
 578 trend initially observed at 875 hPa, (**Fig. 13b**). The enhanced upper-level warming relative to the lower-level led to
 579 a thermally stable stratification, which inhibited vertical mixing and promoted the accumulation of $PM_{2.5}$ near the
 580 surface. In contrast, PM_{10} -polluted days exhibited negative temperature differences below 875 hPa (**Fig. 13d**),
 581 indicating the intrusion of cold air masses. These cold air masses, often accompanied by long-range dust transport,
 582 not only bring in PM_{10} particles from upwind regions but also suppress vertical mixing in the lower atmosphere due
 583 to their higher density. Notably, the altitude of the cooling (875 hPa) coincided with the effective aerosol layer height
 584 identified in our LiDAR-based analyses (**Figs. 8, 11, 12**), which supported the conclusion that dust particles were

585 primarily transported within this level.

586 To further investigate the vertical thermal and humidity differences between clean and polluted days, we focus
 587 on three key pressure levels (1000, 850, and 500 hPa). During PM_{2.5}-polluted periods, the warming at 850 hPa was
 588 greater than that near the surface at 1000 hPa in Hefei (**Fig. S3f&i**). This vertical temperature structure created a
 589 pronounced inversion, which inhibited the vertical mixing and enhanced the atmospheric stability. The lower
 590 troposphere also exhibited elevated relative humidity, particularly in Hefei and nearby regions. Elevated relative
 591 humidity suppresses turbulent exchange and reduces dilution capacity, and hence forms a shallow, moist, and stable
 592 boundary layer that favors pollutant persistence and contributes to poor air quality. In contrast, the clean days showed
 593 a lower humidity in the boundary layer and a weaker vertical temperature gradient, allowing enhanced upward motion
 594 and effective removal of surface aerosols ([Deng et al., 2023](#)). PM₁₀ pollution episodes occurred under a markedly
 595 different meteorological background (**Fig. S4**). Specifically, the relative humidity at both 1000 hPa and 850 hPa was
 596 significantly lower on PM₁₀-polluted days than on clean days (**Fig. S4f&i**). Aloft cold air intrusions occurred on PM₁₀
 597 pollution days, creating favorable conditions for the large-scale transport of dust into Hefei. Under such dry and calm
 598 conditions, ~~the accumulation of PM₁₀~~PM₁₀-accumulation is likely driven by mechanical resuspension or regional dust
 599 transport rather than secondary aerosol formation processes enhanced by moisture ([Li et al., 2020](#)). Overall, these
 600 findings reveal that PM_{2.5} episodes over Hefei are typically governed by moist and thermodynamically stable
 601 boundary layers under subsiding air masses, while PM₁₀ events are more influenced by dust-laden airflow and dry
 602 boundary-layer dynamics. The distinct thermal and humidity structures observed across the vertical profile emphasize
 603 the importance of differentiating pollution types when diagnosing meteorological drivers.

604 The vertical wind velocity was investigated at three pressure levels to reveal the dynamic mechanisms on PM_{2.5}
 605 and PM₁₀ pollution days (**Figs. 14 & 15**). To better elucidate the meteorological characteristics between polluted and
 606 clean conditions, we calculated the differences in vertical velocity between these two scenarios, as their broadly
 607 similar large-scale background circulation patterns obscure the subtle but critical dynamic anomalies that drive
 608 pollution formation. On PM_{2.5}-polluted days, the atmosphere around Hefei exhibits a clear subsidence trend at 850
 609 and 1000 hPa (**Fig. 14**). The subsidence reflects the existence of high-pressure systems and stagnant synoptic
 610 conditions, which contribute to the accumulation of fine particles. This inhibition of the upward motion of vertical
 611 wind corresponds with a stable thermal structure, which can effectively restrict vertical exchange and compress the
 612 boundary layer. During PM₁₀ pollution events, subsidence at 500 hPa is significantly ~~stronger~~greater than ~~on clean~~
 613 ~~days compared to that on~~ clean days (**Fig. 15**). However, ~~However,~~ Hefei is located in a unique region defined by
 614 upward motion at 850 hPa, with a comparable weak upward movement also observed at 1000 hPa. The subsidence

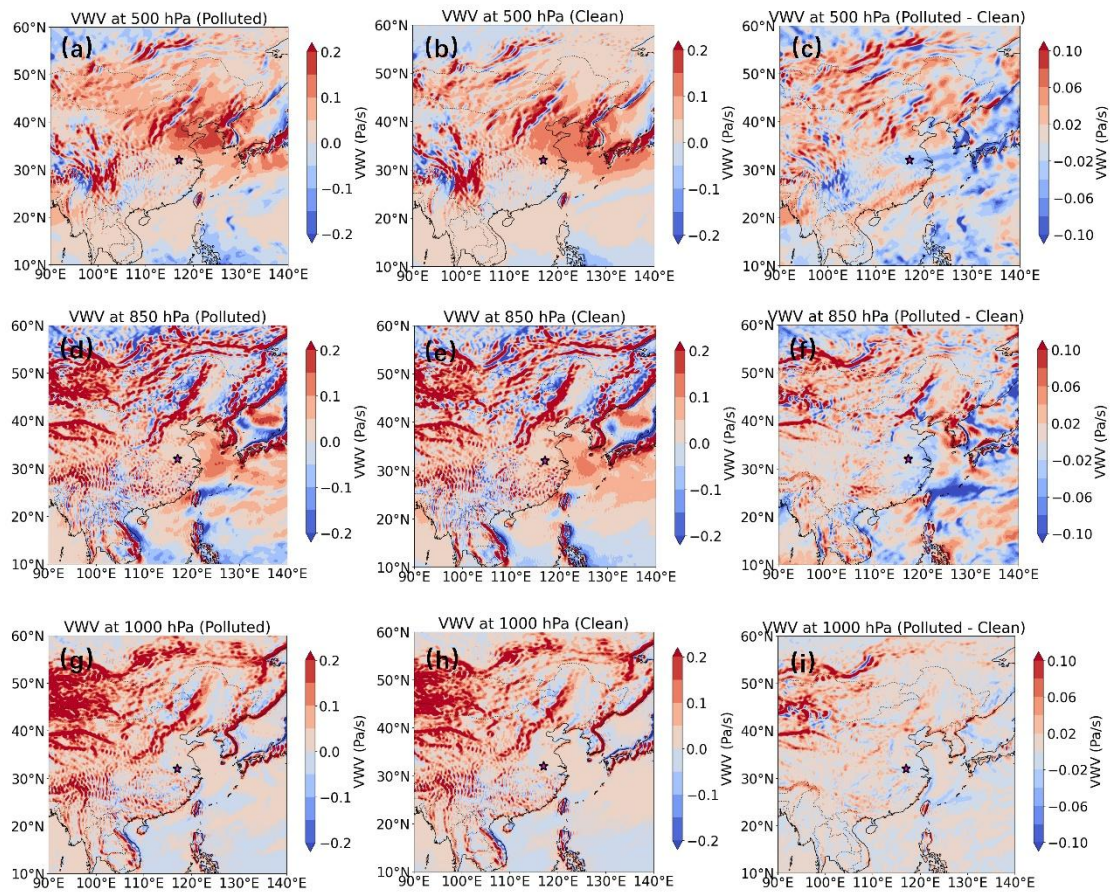
615 at 500 hPa stabilizes the atmosphere and suppresses the upward dispersion of particles. Meanwhile, upward motion
 616 at 850 hPa and near the surface (1000 hPa) may be caused by local convergence or orographic lifting, allowing the
 617 uplift and recirculation of dust within the lower troposphere. This dynamic difference could reflect more complex
 618 interactions between local surface sources and large-scale synoptic. Upward motion at 850 hPa supports the
 619 interpretation that PM_{10} events are influenced by weak convective movements or vertical recycling of particles within
 620 a confined layer rather than stagnation alone. These findings reveal that $PM_{2.5}$ and PM_{10} pollution in Hefei are
 621 governed by contrasting vertical dynamic regimes. $PM_{2.5}$ events are closely tied to a uniformly subsiding atmosphere,
 622 which favors the trapping and accumulation of fine particles. In contrast, PM_{10} events are characterized by a layered
 623 structure, where upper-level subsidence and lower-level ascent work in tandem to recirculate coarse particles, rather
 624 than simply trapping them. This distinction underscores the need for targeted, pollutant-specific strategies in air
 625 quality forecasting and management.



626

627 **Figure 13.** Vertical distributions of temperature for polluted, clean, and their difference in (a, b) $PM_{2.5}$ and (c, d)

628 PM_{10} .



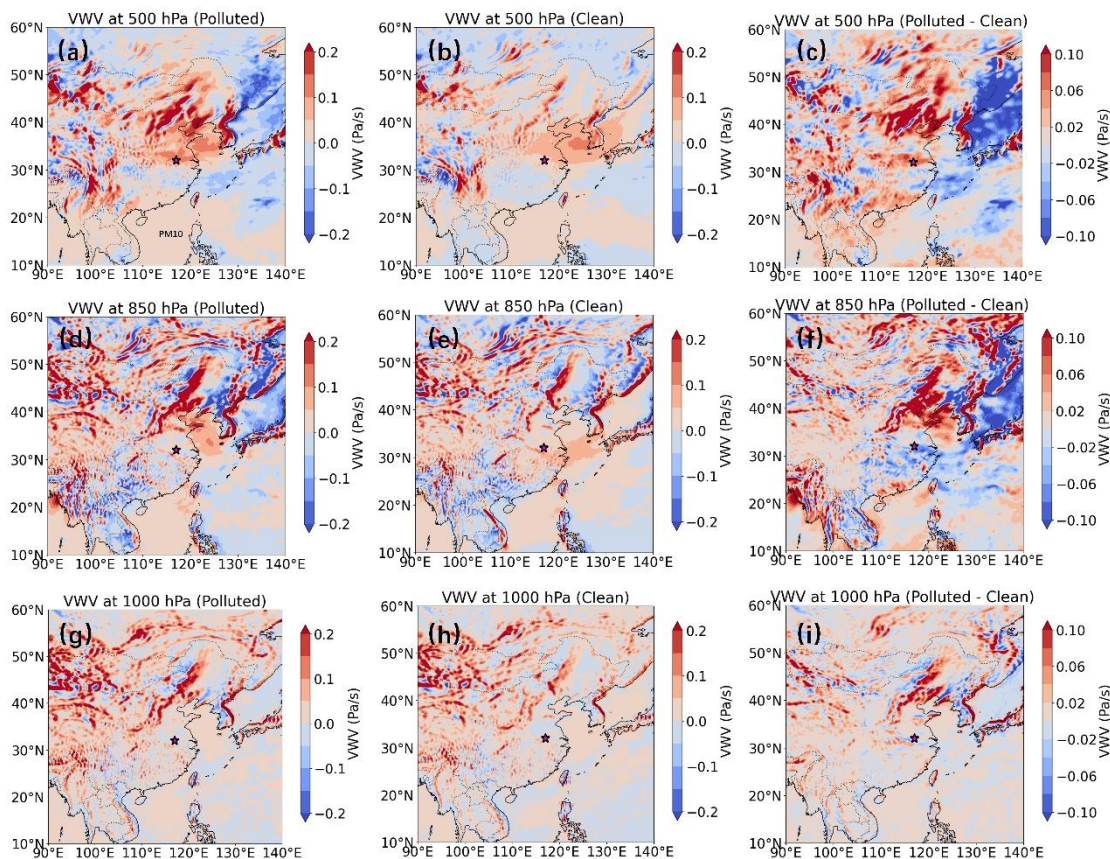
629

630 **Figure 14.** Spatial distribution of the vertical wind velocity (VWV) at three pressure levels (500 hPa: a–c; 850 hPa:631 d–f; 1000 hPa: g–i) on PM_{2.5}-polluted (left column), clean (middle column) days and the difference between them

632 (right column), respectively. The areas highlighted with a red star represents the location of Hefei.

633

634



635

636 **Figure 15.** Same as Fig. 14, but on PM₁₀-polluted (left column), clean (middle column) days and the difference
 637 between them (right column), respectively.

638

639 4. Conclusions

640 This study comprehensively assesses the vertical structures of aerosols in Hefei by comparing fine (PM_{2.5}) and
 641 coarse (PM₁₀) particulate matter on clean and polluted days. We utilized long-term aerosol LiDAR measurements
 642 and reanalysis meteorological data to compare the vertical distribution characteristics of different particulate pollution
 643 types as well as the underlying thermodynamic and dynamic mechanisms that drive their vertical development.
 644 Aerosol extinction coefficients at 532 nm for PM_{2.5} and PM₁₀ were consistently higher on polluted days than on clean
 645 days. Since fine-mode particles predominate the aerosol population on PM_{2.5} pollution days, the depolarization ratios
 646 fell within a range lower than those observed on clean days. In contrast, PM₁₀-polluted days had larger depolarization
 647 ratios than clean days, indicating significant contributions from non-spherical coarse particles.

648 Our findings reveal that the accumulation of PM_{2.5} is closely linked to stable boundary layer structures
 649 characterized by high humidity, weak vertical shear, and a mid-level inversion temperature. These conditions
 650 collectively inhibit vertical exchange and confine fine particles near the surface. The vertical extinction and
 651 depolarization profiles support the dominance of aerosols during PM_{2.5} pollution, particularly in the lower 0.9 km. In

652 contrast, PM_{10} pollution is typically associated with low humidity and mechanically driven transport of dust from
653 upwind sources. The vertical profiles show enhanced depolarization ratios, indicating the presence of non-spherical,
654 coarse particles such as dust or resuspended material. Distinct vertical motion patterns identify the two types of
655 pollution. $PM_{2.5}$ episodes showed upward mobility in the mid-troposphere and near-surface subsidence, which
656 reinforced stratification and pollution trapping. However, PM_{10} events were distinguished by upper-level subsidence
657 coupled with low-level ascent, which might facilitate vertical transport of coarse particles during regional dust
658 episodes. These dynamic differences highlight that $PM_{2.5}$ and PM_{10} are generated by fundamentally separate
659 atmospheric processes, and a unified treatment of particulate pollution risks oversimplifies their behavior.

660 Expanding such analyses across multiple sites would also aid in identifying geographical heterogeneity and
661 testing the generalizability of the discovered trends. Future research may be directed toward integrating long-term,
662 high-resolution vertical observations with advanced modeling approaches to better understand the multiscale
663 dynamics behind various forms of particle pollution and create tailored mitigation solutions.

664

665 **Acknowledgments**

666 This work was supported by the Innovation and Development Special Project of Anhui Meteorological Bureau
667 (CXB202404), the Open Fund Project for Heavy Rain (BYKJ2025D03), the Science and Technology Projects of
668 Xizang Autonomous Region, China (XZ202502JD0041), the Special Project for Forecasters of Anhui Meteorological
669 Bureau (KY202003), and the 2025 Independent Innovation Scientific Research Project of Anhui Public
670 Meteorological Service Center (GFCX202504).

671

672 **Data Availability**

673 Hourly concentrations of major air pollutants were obtained from the China National Environmental Monitoring
674 Centre (CNEMC) (<https://www.cnemc.cn/>). Surface meteorological variables were obtained from the China
675 Meteorological Administration (CMA) (<http://data.cma.cn/en>). The ERA5 reanalysis dataset, used to investigate the
676 impact of synoptic systems on $PM_{2.5}$ and PM_{10} pollution, was freely accessible via the Copernicus Climate Change
677 Services platform (<https://cds.climate.copernicus.eu/datasets>).

678

679 **Author Contribution**

680 X.D. conceived the study; Y.Y. acquired and analyzed the data and drafted the manuscript; R.D. and Q.X.
681 performed data processing and investigation; Q.H., Y.L., and C.W. provided theoretical support; J.X. and Y.S.

682 discussed the results and revised the manuscript; Y.L. acquired funding; all co-authors reviewed and approved the
 683 final version of the manuscript.

684

685 **Competing interests**

686 The authors declare that they have no conflict of interest.

687

688 **References**

- 689 Ansmann, A., Muellera, D., Wandinger, U., & Mamouri, R.E. (2013). Lidar profiling of aerosol optical and microphysical
 690 properties from space: Overview, review, and outlook. In, *1st International Conference on Remote Sensing and*
 691 *Geoinformation of the Environment (RSCy)*. Paphos, CYPRUS
- 692 Biuki, Z.A., Parvin, P., & Aghaei, M. (2022). Satellite remote sensing of particulate matter in the atmosphere of megacities:
 693 A case study of Tehran, Iran. *Atmospheric Pollution Research*, *13*, <http://doi.org/10.1016/j.apr.2022.101545>.
- 694 Cairo, F., Di Liberto, L., Dionisi, D., & Snels, M. (2024). Understanding aerosol-cloud interactions through lidar techniques:
 695 A review. *Remote Sensing*, *16*, <http://doi.org/10.3390/rs16152788>.
- 696 Chen, C., Song, X., Wang, Z., Chen, Y., Wang, X., Bu, Z., Zhang, X., Zhuang, Q., Pan, X., Li, H., Zhang, F., Wang, X., Li,
 697 X., & Zheng, R. (2022). Calibration methods of atmospheric aerosol lidar and a case study of haze process. *Frontiers*
 698 *in Physics*, *10*, <http://doi.org/10.3389/fphy.2022.942926>.
- 699 Chen, W., Tang, H.Z., Zhao, H.M., & Yan, L. (2016). Analysis of aerosol properties in Beijing based on ground-based sun
 700 photometer and air quality monitoring observations from 2005 to 2014. *Remote Sensing*, *8*,
 701 <http://doi.org/10.3390/rs8020110>.
- 702 Chen, X., Yang, T., Wang, H.B., Wang, F.T., & Wang, Z.F. (2023). Variations and drivers of aerosol vertical characterization
 703 after clean air policy in China based on 7-years consecutive observations. *Journal of Environmental Sciences*, *125*,
 704 499-512, <http://doi.org/10.1016/j.jes.2022.02.036>.
- 705 Chen, Y., Bu, Z., Wang, X., Dai, Y., Li, Z., Lu, T., Liu, Y., & Wang, X. (2024a). Development and calibration of 532 nm
 706 standard aerosol lidar with low blind area. *Remote Sensing*, *16*, <http://doi.org/10.3390/rs16030570>.
- 707 Chen, Z., Ji, C., Mao, J., Wang, Z., Jiao, Z., Gao, L., Xiang, Y., & Zhang, T. (2024b). Downdraft influences on the
 708 differences of PM_{2.5} concentration: Insights from a mega haze evolution in the winter of northern China.
 709 *Environmental Research Letters*, *19*, <http://doi.org/10.1088/1748-9326/ad1229>.
- 710 Chouza, F., Reitebuch, O., Gross, S., Rahm, S., Freudenthaler, V., Toledano, C., & Weinzierl, B. (2015). Retrieval of aerosol
 711 backscatter and extinction from airborne coherent Doppler wind lidar measurements. *Atmospheric Measurement*

- 712 *Techniques*, 8, 2909-2926, <http://doi.org/10.5194/amt-8-2909-2015>.
- 713 Dai, F., Chen, M., & Yang, B. (2020). Spatiotemporal variations of PM_{2.5} concentration at the neighborhood level in five
714 Chinese megacities. *Atmospheric Pollution Research*, 11, 190-202, <http://doi.org/10.1016/j.apr.2020.03.010>.
- 715 Deng, X.L., Chen, J., Dai, R., Zhai, Z.F., He, D.Y., Zhao, L., Jin, X.L., & Zhang, J.P. (2023). The effects of planetary
716 boundary layer features on air pollution based on ERA5 data in East China. *Atmosphere*, 14,
717 <http://doi.org/10.3390/atmos14081273>.
- 718 Fan, G., Zhang, B., Zhang, T., Fu, Y., Pei, C., Lou, S., Li, X., Chen, Z., & Liu, W. (2024). Accuracy evaluation of differential
719 absorption lidar for ozone detection and intercomparisons with other instruments. *Remote Sensing*, 16,
720 <http://doi.org/10.3390/rs16132369>.
- 721 Fan, S., Gao, C.Y., Wang, L., Yang, Y., Liu, Z., Hu, B., Wang, Y., Wang, J., & Gao, Z. (2021). Elucidating roles of near-
722 surface vertical layer structure in different stages of PM_{2.5} pollution episodes over urban Beijing during 2004-2016.
723 *Atmospheric Environment*, 246, <http://doi.org/10.1016/j.atmosenv.2020.118157>.
- 724 Fang, Z., Yang, H., Li, C., Kuang, Z., Xu, X., & Jin, H. (2024). Reveal persistent haze pollution episodes in Hefei: A
725 perspective from ground-based and satellite observation. *Air Quality Atmosphere and Health*, 17, 2555-2568,
726 <http://doi.org/10.1007/s11869-024-01587-2>.
- 727 Gao, F., Bergant, K., Filipcic, A., Forte, B., Hua, D.X., Song, X.Q., Stanic, S., Veberic, D., & Zavrtanik, M. (2011).
728 Observations of the atmospheric boundary layer across the land-sea transition zone using a scanning Mie lidar.
729 *Journal of Quantitative Spectroscopy & Radiative Transfer*, 112, 182-188, <http://doi.org/10.1016/j.jqsrt.2010.04.001>.
- 730 Gao, Y.-Q., Chen, Y., Liu, G.-D., & Zhang, J.-M. (2020). Investigating the influence of meteorological factors on particulate
731 matters: A case study based on path analysis. *Energy & Environment*, 31, 479-491,
732 <http://doi.org/10.1177/0958305x19876696>.
- 733 Garratt, J.R. (1994). Review: The atmospheric boundary layer. *Earth-Science Reviews*, 37, 89-134,
734 [http://doi.org/10.1016/0012-8252\(94\)90026-4](http://doi.org/10.1016/0012-8252(94)90026-4).
- 735 Gebauer, H., Floutsi, A.A., Haarig, M., Radenz, M., Engelmann, R., Althausen, D., Skupin, A., Ansmann, A., Zenk, C., &
736 Baars, H. (2024). Tropospheric sulfate from Cumbre Vieja (La Palma) observed over Cabo Verde contrasted with
737 background conditions: A lidar case study of aerosol extinction, backscatter, depolarization and lidar ratio profiles
738 at 355, 532 and 1064 nm. *Atmospheric Chemistry and Physics*, 24, 5047-5067, [http://doi.org/10.5194/acp-24-5047-](http://doi.org/10.5194/acp-24-5047-2024)
739 [2024](http://doi.org/10.5194/acp-24-5047-2024).
- 740 Haarig, M., Ansmann, A., Gasteiger, J., Kandler, K., Althausen, D., Baars, H., Radenz, M., & Farrell, D.A. (2017). Dry
741 versus wet marine particle optical properties: RH dependence of depolarization ratio, backscatter, and extinction

- 742 from multiwavelength lidar measurements during SALTRACE. *Atmospheric Chemistry and Physics*, 17, 14199-
743 14217, <http://doi.org/10.5194/acp-17-14199-2017>.
- 744 Han, X., & Cao, T. (2022). Urbanization level, industrial structure adjustment and spatial effect of urban haze pollution:
745 Evidence from China's Yangtze River Delta urban agglomeration. *Atmospheric Pollution Research*, 13,
746 <http://doi.org/10.1016/j.apr.2022.101427>.
- 747 [He, G., Deng, T., Wu, D., Wu, C., Huang, X., Li, Z., Yin, C., Zou, Y., Song, L., Ouyang, S., Tao, L., & Zhang, X. \(2021\).
748 Characteristics of boundary layer ozone and its effect on surface ozone concentration in Shenzhen, China: A case
749 study. *Science of the Total Environment*, 791, <https://doi.org/10.1016/j.scitotenv.2021.148044>.](#)
- 750 He, Y., Li, L., Wang, H., Xu, X., Li, Y., & Fan, S. (2022). A cold front induced co-occurrence of O₃ and PM_{2.5} pollution in
751 a Pearl River Delta city: Temporal variation, vertical structure, and mechanism. *Environmental Pollution*, 306,
752 <http://doi.org/10.1016/j.envpol.2022.119464>.
- 753 Huang, L., Chen, M.D., & Hu, J.L. (2016). Twelve-year trends of PM₁₀ and visibility in the Hefei metropolitan area of
754 China. *Advances in Meteorology*, 2016, <http://doi.org/10.1155/2016/4810796>.
- 755 Jin, X., Cai, X., Yu, M., Wang, X., Song, Y., Kang, L., Zhang, H., & Zhu, T. (2021). Mesoscale structure of the atmospheric
756 boundary layer and its impact on regional air pollution: A case study. *Atmospheric Environment*, 258,
757 <http://doi.org/10.1016/j.atmosenv.2021.118511>.
- 758 Kumar, V.R., Collins, R.L., & Yellapragada, B.K. (2024). Polarization lidar observations of diurnal and seasonal variations
759 in the atmospheric mixing layer above a tropical rural place gadanki, India. *Journal of Atmospheric and Solar-
760 Terrestrial Physics*, 263, <http://doi.org/10.1016/j.jastp.2024.106335>.
- 761 Li, H.D., Sodoudi, S., Liu, J.F., & Tao, W. (2020). Temporal variation of urban aerosol pollution island and its relationship
762 with urban heat island. *Atmospheric Research*, 241, <http://doi.org/10.1016/j.atmosres.2020.104957>.
- 763 Li, Q.H., Zhang, H.S., Jin, X.P., Cai, X.H., & Song, Y. (2022). Mechanism of haze pollution in summer and its difference
764 with winter in the North China Plain. *Science of the Total Environment*, 806,
765 <http://doi.org/10.1016/j.scitotenv.2021.150625>.
- 766 Li, X., Wang, Y., Shen, L., Zhang, H., Zhao, H., Zhang, Y., & Ma, Y. (2018). Characteristics of boundary layer structure
767 during a persistent haze event in the central Liaoning city Cluster, Northeast China. *Journal of Meteorological
768 Research*, 32, 302-312, <http://doi.org/10.1007/s13351-018-7053-6>.
- 769 Li, Y., Chen, Q.L., Zhao, H.J., Wang, L., & Tao, R. (2015). Variations in PM₁₀, PM_{2.5} and PM_{1.0} in an urban area of the
770 Sichuan basin and their relation to meteorological factors. *Atmosphere*, 6, 150-163,
771 <http://doi.org/10.3390/atmos6010150>.

- 772 Li, Y., Huang, T., Lee, H.F., Heo, Y., Ho, K.-F., & Yim, S.H.L. (2024). Integrating Doppler lidar and machine learning into
773 land-use regression model for assessing contribution of vertical atmospheric processes to urban PM_{2.5} pollution.
774 *Science of the Total Environment*, 952, <http://doi.org/10.1016/j.scitotenv.2024.175632>.
- 775 Liu, C., Huang, J., Wang, Y., Tao, X., Hu, C., Deng, L., Xu, J., Xiao, H.-W., Luo, L., Xiao, H.-Y., & Xiao, W. (2020).
776 Vertical distribution of PM_{2.5} and interactions with the atmospheric boundary layer during the development stage of
777 a heavy haze pollution event. *Science of the Total Environment*, 704, <http://doi.org/10.1016/j.scitotenv.2019.135329>.
- 778 Liu, J.L., Cai, P.L., Dong, J., Wang, J.S., Li, R.K., & Song, X.F. (2021). Assessment of the dynamic exposure to PM_{2.5}
779 based on hourly cell phone location and land use regression model in Beijing. *International Journal of*
780 *Environmental Research and Public Health*, 18, <http://doi.org/10.3390/ijerph18115884>.
- 781 Liu, T.T., Gong, S.L., He, J.J., Yu, M., Wang, Q.F., Li, H.R., Liu, W., Zhang, J., Li, L., Wang, X.G., Li, S.L., Lu, Y.L., Du,
782 H.T., Wang, Y.Q., Zhou, C.H., Liu, H.L., & Zhao, Q.C. (2017). Attributions of meteorological and emission factors
783 to the 2015 winter severe haze pollution episodes in China's Jing-Jin-Ji area. *Atmospheric Chemistry and Physics*,
784 17, 2971-2980, <http://doi.org/10.5194/acp-17-2971-2017>.
- 785 Liu, Z., Xiang, Y., Pan, Y., Zhang, T., Xu, W., & Li, L. (2024). Unveiling 3-D evolution and mechanisms of ozone pollution
786 in Changzhou, China: Insights from lidar observations and modelling. *Environmental Pollution*, 359, 124556,
787 <http://doi.org/10.1016/j.envpol.2024.124556>.
- 788 Liu, Z.R., Hu, B., Wang, L.L., Wu, F.K., Gao, W.K., & Wang, Y.S. (2015). Seasonal and diurnal variation in particulate
789 matter (PM₁₀ and PM_{2.5}) at an urban site of Beijing: analyses from a 9-year study. *Environmental Science and*
790 *Pollution Research*, 22, 627-642, <http://doi.org/10.1007/s11356-014-3347-0>.
- 791 Ma, P., Zhang, Z., Zhang, Y., Lamu, Y., & Za, D. (2023). Effect of meteorological conditions on PM₁₀ concentrations in
792 the middle reaches of the Yarlung Zangbo River, Tibet Plateau. *Theoretical and Applied Climatology*, 151, 725-737,
793 <http://doi.org/10.1007/s00704-022-04330-y>.
- 794 Mehta, M., Khushboo, R., Raj, R., & Singh, N. (2021). Spaceborne observations of aerosol vertical distribution over Indian
795 mainland (2009-2018). *Atmospheric Environment*, 244, <http://doi.org/10.1016/j.atmosenv.2020.117902>.
- 796 Miao, Y.C., Guo, J.P., Liu, S.H., Zhao, C., Li, X.L., Zhang, G., Wei, W., & Ma, Y.J. (2018). Impacts of synoptic condition
797 and planetary boundary layer structure on the trans-boundary aerosol transport from Beijing-Tianjin-Hebei region
798 to northeast China. *Atmospheric Environment*, 181, 1-11, <http://doi.org/10.1016/j.atmosenv.2018.03.005>.
- 799 Mishra, A.K., & Shibata, T. (2012). Climatological aspects of seasonal variation of aerosol vertical distribution over central
800 Indo-Gangetic belt (IGB) inferred by the space-borne lidar CALIOP. *Atmospheric Environment*, 46, 365-375,
801 <http://doi.org/10.1016/j.atmosenv.2011.09.052>.

- 802 Ou, J., Hu, Q., Liu, H., Hong, Q., Xing, C., Tan, W., Lin, H., Wang, X., Xu, H., Zhu, P., & Liu, W. (2021). Vertical
803 characterization and potential sources of aerosols in different seasons over the Yangtze River Delta using ground-
804 based MAX-DOAS. *Environmental Pollution*, 279, <http://doi.org/10.1016/j.envpol.2021.116898>.
- 805 Qian, Z., Li, L., Lin, X., Sun, R., & Chen, Y. (2024). Spatial and temporal variation of PM_{2.5} and the influence of vegetation
806 in the Yangtze River Delta region. *Atmospheric Pollution Research*, 15, <http://doi.org/10.1016/j.apr.2024.102266>.
- 807 Shen, L., Cheng, Y., Bai, X., Dai, H., Wei, X., Sun, L., Yang, Y., Zhang, J., Feng, Y., Li, Y.J., Chen, D.-R., Liu, J., & Gui,
808 H. (2022). Vertical profile of aerosol number size distribution during a haze pollution episode in Hefei, China.
809 *Science of the Total Environment*, 814, <http://doi.org/10.1016/j.scitotenv.2021.152693>.
- 810 Shi, C.N., Yuan, R.M., Wu, B.W., Meng, Y.J., Zhang, H., Zhang, H.Q., & Gong, Z.Q. (2018). Meteorological conditions
811 conducive to PM_{2.5} pollution in winter 2016/2017 in the Western Yangtze River Delta, China. *Science of the Total*
812 *Environment*, 642, 1221-1232, <http://doi.org/10.1016/j.scitotenv.2018.06.137>.
- 813 Shim, K., Kim, M.-H., Lee, H.-J., Nishizawa, T., Shimizu, A., Kobayashi, H., Kim, C.-H., & Kim, S.-W. (2022).
814 Exacerbation of PM_{2.5} concentration due to unpredictable weak Asian dust storm: A case study of an extraordinarily
815 long-lasting spring haze episode in Seoul, Korea. *Atmospheric Environment*, 287,
816 <http://doi.org/10.1016/j.atmosenv.2022.119261>.
- 817 Sun, W.B., Liu, Z.Y., Videen, G., Fu, Q., Muinonen, K., Winker, D.M., Lukashin, C., Jin, Z.H., Lin, B., & Huang, J.P.
818 (2013). For the depolarization of linearly polarized light by smoke particles. *Journal of Quantitative Spectroscopy*
819 *& Radiative Transfer*, 122, 233-237, <http://doi.org/10.1016/j.jqsrt.2012.03.031>.
- 820 Sun, X., Zhao, T., Hu, J., Bai, Y., Meng, L., Yang, Q., Zhou, Y., & Fu, W. (2024a). Inverse effects of aerosol radiative
821 forcing on heavy PM_{2.5} pollution of local accumulation and regional transport over central China. *Science of the*
822 *Total Environment*, 917, <http://doi.org/10.1016/j.scitotenv.2024.170319>.
- 823 Sun, X., Zhou, Y., Zhao, T., Fu, W., Wang, Z., Shi, C., Zhang, H., Zhang, Y., Yang, Q., & Shu, Z. (2024b). Vertical
824 distribution of aerosols and association with atmospheric boundary layer structures during regional aerosol transport
825 over central China. *Environmental Pollution*, 362, <http://doi.org/10.1016/j.envpol.2024.124967>.
- 826 Tombrou, M., Dandou, A., Helmis, C., Akylas, E., Angelopoulos, G., Flocas, H., Assimakopoulos, V., & Soulakellis, N.
827 (2007). Model evaluation of the atmospheric boundary layer and mixed-layer evolution. *Boundary-Layer*
828 *Meteorology*, 124, 61-79, <http://doi.org/10.1007/s10546-006-9146-5>.
- 829 Vakkari, V., Baars, H., Bohlmann, S., Bühl, J., Komppula, M., Mamouri, R.-E., & O'Connor, E.J. (2021). Aerosol particle
830 depolarization ratio at 1565 nm measured with a Halo Doppler lidar. *Atmospheric Chemistry and Physics*, 21, 5807-
831 5820, <http://doi.org/10.5194/acp-21-5807-2021>.

- 832 Wang, H., Sun, Z., Li, H., Gao, Y., Wu, J., & Cheng, T. (2018). Vertical-distribution characteristics of atmospheric aerosols
833 under different thermodynamic conditions in Beijing. *Aerosol and Air Quality Research*, *18*, 2775-2787,
834 <http://doi.org/10.4209/aaqr.2018.03.0078>.
- 835 Wang, J., Wang, H., Zhang, C., Wang, Y., Zhang, Y., Zhou, J., Xu, W., Whalley, L.K., Dyson, J.E., Slater, E.J., Xing, C.,
836 Chi, S., Wang, Y., Wang, L., Yu, X., Zeng, L., Lin, W., Zhao, W., Heard, D.E., Song, S., & Ye, C. (2025). Ozone
837 production underestimation over the Tibetan Plateau: The role of NO_x and OVOCs modeling uncertainties. *Journal*
838 *of Geophysical Research-Atmospheres*, *130*, <http://doi.org/10.1029/2025jd043321>.
- 839 Wang, J.L., Zhang, Y.H., Shao, M., Liu, X.L., Zeng, L.M., Cheng, C.L., & Xu, X.F. (2004). Chemical composition and
840 quantitative relationship, between meteorological condition and fine particles in Beijing. *Journal of Environmental*
841 *Sciences*, *16*, 860-864
- 842 Wang, L.Y., Lyu, B.L., & Bai, Y.Q. (2020a). Aerosol vertical profile variations with seasons, air mass movements and local
843 PM_{2.5} levels in three large China cities. *Atmospheric Environment*, *224*,
844 <http://doi.org/10.1016/j.atmosenv.2020.117329>.
- 845 Wang, M., & Wang, H. (2021). Spatial distribution patterns and influencing factors of PM_{2.5} pollution in the Yangtze River
846 Delta: Empirical analysis based on a GWR model. *Asia-Pacific Journal of Atmospheric Sciences*, *57*, 63-75,
847 <http://doi.org/10.1007/s13143-019-00153-6>.
- 848 Wang, M., Wei, T., Lolli, S., Wu, K., Wang, Y., Hu, H., Yuan, J., Tang, D., & Xia, H. (2024). A long-term Doppler wind
849 lidar study of heavy pollution episodes in western Yangtze River Delta region, China. *Atmospheric Research*, *310*,
850 <http://doi.org/10.1016/j.atmosres.2024.107616>.
- 851 Wang, Z., Liu, C., Hu, Q.H., Dong, Y.S., Liu, H.R., Xing, C.Z., & Tan, W. (2021). Quantify the Contribution of Dust and
852 Anthropogenic Sources to Aerosols in North China by Lidar and Validated with CALIPSO. *Remote Sensing*, *13*,
853 <http://doi.org/10.3390/rs13091811>.
- 854 Wang, Z., Liu, C., Xie, Z.Q., Hu, Q.H., Andreae, M.O., Dong, Y.S., Zhao, C., Liu, T., Zhu, Y.Z., Liu, H.R., Xing, C.Z., Tan,
855 W., Ji, X.G., Lin, J.N., & Liu, J.G. (2020b). Elevated dust layers inhibit dissipation of heavy anthropogenic surface
856 air pollution. *Atmospheric Chemistry and Physics*, *20*, 14917-14932, <http://doi.org/10.5194/acp-20-14917-2020>.
- 857 Xiang, Y., Zhang, T., Liu, J., Wan, X., Loewen, M., Chen, X., Kang, S., Fu, Y., Lv, L., Liu, W., & Cong, Z. (2021). Vertical
858 profile of aerosols in the Himalayas revealed by lidar: New insights into their seasonal/diurnal patterns, sources,
859 and transport*. *Environmental Pollution*, *285*, <http://doi.org/10.1016/j.envpol.2021.117686>.
- 860 Xiong, K., Xie, X., Mao, J., Wang, K., Huang, L., Li, J., & Hu, J. (2023). Improving the accuracy of O₃ prediction from a
861 chemical transport model with a random forest model in the River Delta China. *Environmental Pollution*, *319*,

- 862 <http://doi.org/10.1016/j.envpol.2022.120926>.
- 863 Yang, S.M., Ma, Y.J., Zhang, W.Y., Lin, Z., Lu, Z.G., Zhou, X.J., Ren, Y.Z., Ren, X.B., Peng, K.C., Tan, Y.L., Wei, Y.M.,
864 Ahmad, M., Zhao, D.D., Kong, L.B., Ma, Y.N., Tian, Y.L., & Xin, J.Y. (2025). The interaction of atmospheric
865 boundary layer and PM pollution in Mongolian Plateau: Implication for the threshold control strategy. *Atmospheric*
866 *Research*, 316, <http://doi.org/10.1016/j.atmosres.2025.107937>.
- 867 Yang, Y.J., Yim, S.H.L., Haywood, J., Osborne, M., Chan, J.C.S., Zeng, Z.L., & Cheng, J.C.H. (2019). Characteristics of
868 heavy particulate matter pollution events over Hong Kong and their relationships with vertical wind profiles using
869 high-time-resolution Doppler lidar measurements. *Journal of Geophysical Research-Atmospheres*, 124, 9609-9623,
870 <http://doi.org/10.1029/2019jd031140>.
- 871 Yang, Z., Wang, Y., Xu, X.-H., Yang, J., & Ou, C.-Q. (2022). Quantifying and characterizing the impacts of PM_{2.5} and
872 humidity on atmospheric visibility in 182 Chinese cities: A nationwide time-series study. *Journal of Cleaner*
873 *Production*, 368, <http://doi.org/10.1016/j.jclepro.2022.133182>.
- 874 Yu, H.J., Wang, Y.J., Peng, Q., Shao, Y.Q., Duan, C.M., Zhu, Y.F., Dong, S.R., Li, C.L., Shi, Y., Zhang, N., Zheng, Y.Y.,
875 Chen, Y., Jiang, Q.W., Zhong, P.S., & Zhou, Y.B. (2020). Influence of coarse particulate matter on chickenpox in
876 Jiading District, Shanghai, 2009-2018: A distributed lag non-linear time series analysis. *Environmental Research*,
877 190, <http://doi.org/10.1016/j.envres.2020.110039>.
- 878 Yu, S., Liu, D., Xu, J., Wang, Z., Wu, D., Shan, Y., Shao, J., Mao, M., Qian, L., Wang, B., Xie, C., & Wang, Y. (2021).
879 Optical properties and seasonal distribution of aerosol layers observed by lidar over Jinhua, southeast China.
880 *Atmospheric Environment*, 257, <http://doi.org/10.1016/j.atmosenv.2021.118456>.
- 881 Zhan, Y., Xie, M., Zhuang, B., Gao, D., Zhu, K., Lu, H., Wang, T., Li, S., Li, M., Luo, Y., & Zhao, R. (2024). Particle-
882 ozone complex pollution under diverse synoptic weather patterns in the Yangtze River Delta region: Synergistic
883 relationships and the effects of meteorology and chemical compositions. *Science of the Total Environment*, 946,
884 174365, <http://doi.org/10.1016/j.scitotenv.2024.174365>.
- 885 Zhang, T., Che, H.Z., Gong, Z.Q., Wang, Y.Q., Wang, J.Z., Yang, Y.Q., Gui, K., & Guo, B. (2020a). The two-way feedback
886 effect between aerosol pollution and planetary boundary layer structure on the explosive rise of PM_{2.5} after the "Ten
887 Statements of Atmosphere" in Beijing. *Science of the Total Environment*, 709,
888 <http://doi.org/10.1016/j.scitotenv.2019.136259>.
- 889 Zhang, Y., Guo, J., Yang, Y., Wang, Y., & Yim, S.H.L. (2020b). Vertical wind shear modulates particulate matter pollutions:
890 A perspective from radar wind profiler observations in Beijing, China. *Remote Sensing*, 12,
891 <http://doi.org/10.3390/rs12030546>.

892 Zhong, J., Zhang, X., Dong, Y., Wang, Y., Liu, C., Wang, J., Zhang, Y., & Che, H. (2018). Feedback effects of boundary-
893 layer meteorological factors on cumulative explosive growth of PM_{2.5} during winter heavy pollution episodes in
894 Beijing from 2013 to 2016. *Atmospheric Chemistry and Physics*, 18, 247-258, [http://doi.org/10.5194/acp-18-247-](http://doi.org/10.5194/acp-18-247-2018)
895 [2018](http://doi.org/10.5194/acp-18-247-2018).
896